UNIVERSITY OF CALIFORNIA SAN DIEGO

Cameraless High-throughput Imaging Flow Cytometry for Biomedical Applications

A dissertation submitted in partial satisfaction

of the requirements for the degree

Doctor of Philosophy

in

Electrical Engineering (Photonics)

by

Yuanyuan Han

Committee in charge:

Professor Yu-Hwa Lo, Chair
Professor Tse Nga Ng, Co-Chair
Professor Zhaowei Liu
Professor Truong Nguyen
Professor Bing Ren
Professor Yingxiao Wang

2019

The Dissertation of Yuanyuan Han is approved, and it is acceptable in quality and form for publication on microfilm and electronically:

_____

_____

_____

_____

_____

Co-Chair

_____

Chair

University of California San Diego

2019

DEDICATION

To my husband Qian and our parents

EPIGRAPH

History repeats, but science reverberates.

—Siddhartha Mukherjee

Keep it simple, stupid.

—Kelly Johnson

TABLE OF CONTENTS

LIST OF FIGURES

LIST OF TABLES

ACKNOWLEDGEMENTS

First and foremost, I would like to express my sincere gratitude to my advisor, Prof. Yu-Hwa Lo, for his immeasurable amount of support and guidance throughout my Ph.D. research and study. He introduced me to an exciting research area of biomedical devices. During the past 5 years, his patience, vast and deep knowledge of numerous fields, and attention to fundamentals have always inspired me. His training and continual encouragement have allowed me to work towards the success of research projects. His enthusiasm, persistence and optimism have significantly influenced my character both in professional and personal life.

I would also like to thank my committee members, Prof. Tina Ng, Prof. Zhaowei Liu, Prof. Yingxiao (Peter) Wang, Prof. Truong Nguyen, and Prof. Bing Ren for their invaluable time and feedback. I am grateful that they shared their knowledge and experience with me and kept me on the right track during the pursuit of my Ph.D. degree.

Wholeheartedly, I thank impressive former members of Prof. Lo's research group, who I have learned a lot from. Specifically, Dr. Tsung-Feng Wu gave me the great first impression of working on an interdisciplinary research project; Dr. Sunghwan Cho had a significant influence on shaping me into an engineer. Also, I am very thankful to Dr. Yu-Jui (Roger) Chiu, Dr. Zhe (Jerry) Mei, Dr. Tiantian Zhang, Dr. Ti-Hsuan (Leon) Ku, and Dr. Tony Yen for the helpful discussions that we had. I am appreciative of the amazing students Prof. Lo has gathered together in his group. Working daily with such people has made my time in graduate school such a memorable and worthwhile experience. I wish to thank Alex Ce Zhang, Yi Gu, Rui Tang, Wei Cai, Yi-Huan (Jill) Tsai, Ramkumar

Subramanian, Ping-Wei Chen, Violet Castor, Brian Lewis, and Chi-Yang Tseng. I would like to express my appreciation for the help of our collaborators, Dr. Jose Morachis, Dr. William Alaynick, and Constance Ardila at NanoCellect Biomedical, Inc.

Furthermore, I would like to thank my friends for sharing their happiness with me.

I owe thanks to my lovely husband, Qian Ma for his unfailing love. You helped me to keep things in perspective. I greatly value his contribution and deeply appreciate his belief in me. My heart felt regard goes to my mother in law, father in law for their love and moral support.

Most important of all, I am supremely grateful to my family for their unwavering love and support. Especially to my mom, Chunxia Zhang, and my dad, Fengchen Han, you have been the constant thread throughout my entire life. I salute you all for showing faith in me and giving me liberty to choose what I desired. Thank you for always being there.

Chapter 1, in part, is a reprint of the material as it appears in *Lab on a Chip* 2016, Y. Han, Y. Gu, A. C. Zhang, and Y.-H. Lo. "Review: imaging technologies for flow cytometry". The dissertation author was the first author of this paper.

Chapter 2, in part, is a reprint of the material as it appears in *Scientific Reports* 2015, Y. Han and Y.-H. Lo. "Imaging cells in flow cytometry using Spatial Temporal Transformation". The dissertation author was the first author of this paper.

Chapter 2, in part, is a reprint of the material as it appears in *Proceedings of SPIE* 2016, Y. Han and Y.-H. Lo. "Imaging flow cytometer using computation and spatially coded filter". The dissertation author was the first author of this paper.

Chapter 3, in part, has been submitted for publication of the material, Y. Han, R. Tang, Y. Gu, A. C. Zhang, W. Cai, V. Castor, S. H. Cho, W. Alaynick, and Y.-H. Lo. “Cameraless high-throughput 3D imaging flow cytometry”. The dissertation author was the first author of this paper.

VITA

2012	Bachelor of Science, The University of Tulsa
2013-2018	Teaching Assistant, University of California San Diego
2013-2019	Graduate Student Researcher, University of California San Diego
2015	Master of Science, University of California San Diego
2019	Doctor of Philosophy, University of California San Diego

PUBLICATIONS

TF Wu, TM Yen, **Y Han**, YJ Chiu, EYS Lin and YH Lo, "A light-sheet microscope compatible with mobile devices for label-free intracellular imaging and biosensing," *Lab on a Chip*, 14 (17), 3341-3348 (2014).

Y Han and YH Lo, "Imaging cells in flow cytometer using spatial-temporal transformation," *Scientific Reports*, 5, 13267 (2015).

TH Ku, T Zhang, H Luo, TM Yen, PW Chen, **Y Han** and YH Lo, "Nucleic acid aptamers: an emerging tool for biotechnology and biomedical sensing," *Sensors*, 15 (7), 16281-16313 (2015).

AC Zhang, Y Gu, **Y Han**, Z Mei, YJ Chiu, L Geng, SH Cho and YH Lo, "Computational cell analysis for label-free detection of cell properties in a microfluidic laminar flow," *Analyst*, 141 (13), 4142-4150 (2016).

Y Han, Y Gu, AC Zhang and YH Lo, "Imaging technologies for flow cytometry," *Lab on a Chip*, 16 (24), 4639-4647 (2016).

Y Han and YH Lo, "Imaging flow cytometer using computation and spatially coded filter," *Proceedings of SPIE*, 9720, 972010 (2016).

T Zhang, TH Ku, **Y Han**, R Subramanian, IA Niaz, H Luo, D Chang, JJ Huang and YH Lo. "Transient Induced Molecular Electronic Spectroscopy (TIMES) for study of protein-ligand interactions," *Scientific Reports*, 6, 35570 (2016).

T Zhang, T Wei, **Y Han**, H Ma, M Samieegohar, PW Chen, I Lian and YH Lo. "Protein–Ligand Interaction Detection with a Novel Method of Transient Induced Molecular

Electronic Spectroscopy (TIMES): Experimental and Theoretical Studies," *ACS Central Science*, 2 (11), 834-842 (2016).

Y Han, R Tang, Y Gu, AC Zhang, W Cai, V Castor, SH Cho, W Alaynick, and YH Lo, "Cameraless high-throughput 3D imaging flow cytometry," Paper submitted.

PATENTS

YH Lo and **Y Han**, "Imaging flow cytometer using spatial-temporal transformation," U.S. Patent Application (PCT/US2015/053368), September 2015.

YH Lo, **Y Han**, Y Gu and AC Zhang, "Image-based cell sorting systems and methods," U.S. Patent Application (PCT/US2017/036864), June 2017.

YH Lo, T Zhang, TH Ku and **Y Han**, "Transient induced molecular electronic spectroscopy method for study of molecule interactions," U.S. Patent Application (PCT/US2017/021486), March, 2017

YH Lo and **Y Han**, "3D imaging flow cytometer," Submitted to UCSD Office of Innovation and Commercialization on September 28, 2017.

FIELDS OF STUDY

Major Field: Engineering

Studies in Electrical Engineering (Photonics)
Professor Yu-Hwa Lo

ABSTRACT OF THE DISSERTATION

Cameraless High-throughput Imaging Flow Cytometer

for Biomedical Applications

by

Yuanyuan Han

Doctor of Philosophy in Electrical Engineering (Photonics)

University of California San Diego, 2019

Professor Yu-Hwa Lo, Chair
Professor Tina Ng, Co-Chair

High-throughput optical sensing and imaging instrument for capture and analysis of cells are among the most essential tools for biomedical applications. While optical

microscopy is one of the most widely used methods for unveiling the molecular composition of biological specimens, flow cytometry is the gold standard high-throughput tool for single-cell characterization in numerous biomedical and clinical applications. The strong desire to fill in the technological gap between the high-content fluorescence microscope and high-throughput flow cytometer has inspired us to develop a cell analyzer platform with three-dimensional (3D) imaging capabilities.

This dissertation details the development of a 3D imaging flow cytometer, in which microfluidics, acousto-optical, optical and electronic systems are integrated. Based on one enabling technology, namely spatial-temporal transformation, we first developed a novel high-throughput two-dimensional imaging tool for flow cytometry applications. Instead of replacing the single-pixel photodetectors commonly used in flow cytometry with mega-pixelated cameras, this technology uses mathematical algorithms and a specially designed spatial filter to give flow cytometers capabilities of high-throughput, motion-blur-free, multi-color, and multi-mode imaging of single cells. By virtue of the simplicity, high flexibility, and high scalability of this technology, we then combined it with optical sectioning and high-speed laser scanning techniques to enable 3D fluorescence and 90-degree side-scattering imaging of single cells at flow speeds as high as a meter per second. The cameraless 3D imaging flow cytometry uses multiple scanning techniques to add spatial information in a fairly conventional flow cytometry architecture amenable to wide adoption. By precisely mapping time to space, photodetector readout at one timepoint corresponds to one voxel in a 3D space. Through experiments on various biological samples, we demonstrate the functionality of the 3D imaging flow cytometry platform.

As big data create a bonanza for scientists and image-based cell sorter has been brought about, such a high-throughput 3D imaging flow cytometry system will be an enabler to connect phenotype and genotype studies in the fields of immunology, oncology, cell- and gene- therapy, and drug discovery, where heterogeneity is recognized.

Chapter 1

Introduction to Imaging Flow Cytometry

Optical instruments are widely used when high-speed non-invasive measurements are required. Especially in biological, pharmaceutical and medical fields, increasing demand for understanding the vast heterogeneity of cellular phenotypes has driven the development of imaging flow cytometry (IFC), which is a combinatorial platform with features of both flow cytometry and fluorescent microscopy. Before jumping directly into the technical details of imaging flow cytometry, some of its background will be introduced; some of the existing technologies will be reviewed, and their limitations will be discussed. Finally in this chapter, a brief introduction of how the work in this dissertation was carried out will be given.

1.1 Introduction to Flow Cytometry

Flow cytometry is a widespread and powerful technique employed in cell counting, biomarker detection and cell sorting. After the Coulter Principle was discovered in 1953 and Fulwyler applied this principle to sort cells in 1965, optical detections were soon adopted by flow cytometry and fluorescence activated cell sorter (FACS) systems since the late 1960's (1, 2). Figure 1.1 shows a schematic diagram of the fluidic and optical

components of a flow cytometer. Flow cytometry measures optical and fluorescence characteristics of single cells: cells in suspension are drawn into a stream created by a surrounding sheath of isotonic fluid that creates laminar flow, allowing the cells to pass individually through an interrogation point where a laser beam intersects the cells. Emitted and scattered light is collected via optics that direct the light to a series of filters and dichroic mirrors that isolate particular wavelength bands, and detected by photomultiplier tubes and digitized for analysis.

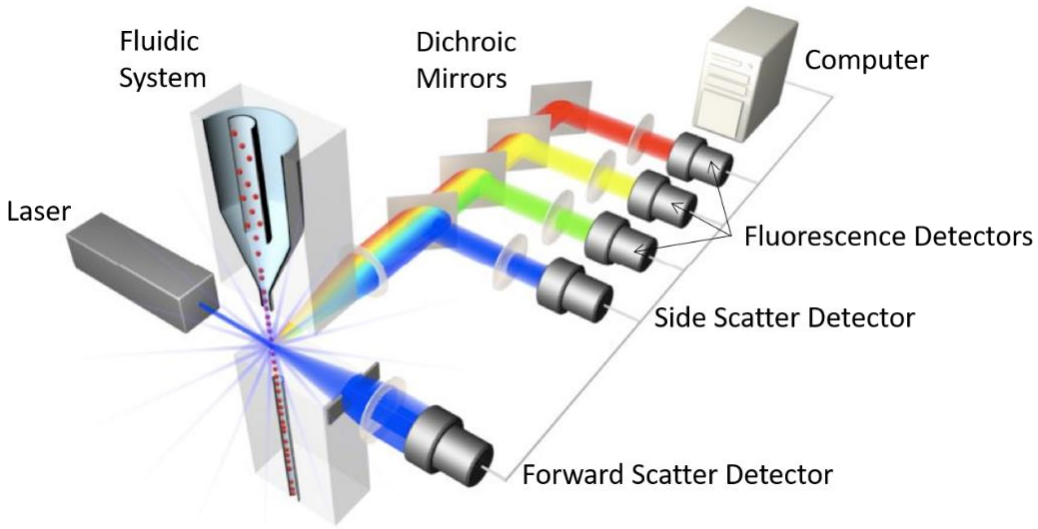

Figure 1.1 Schematic of a flow cytometer.

1.2 Motivation of Obtaining Cell Images in Flow Cytometry

By supporting detection of single cell properties at rates from hundreds to 100,000 cells per second, conventional flow cytometry is an irreplaceable cytologic instrumentation when study of high-volume cell populations and subpopulations needs to be performed due to its high-throughput and multiparametric analysis (3–5). Flow cytometry has found successful applications in immunology and thanks to the growing appreciation of

researchers for the complexity of the immune system, further technological advances has focused on satisfying the increasing need for polychromatic approaches to flow cytometry; researchers have developed flow cytometry to simultaneously measure 19 parameters—17 fluorescence and 2 scatter parameters in a high-speed manner (6). In the meanwhile, false positive occurrence became a concern in flow cytometry. Lacking spatial resolution in exchange for higher throughput in conventional flow cytometry, users have to make gating decisions blind to some of the most informative and relevant sample attributes contained in cell images (7–9). Imaging-in-flow techniques, including flying spot scanner, slit-imaging onto an array, laser strobe, and mirror tracking, were seen as invaluable in understanding the discrepancies in cell measurements due to cell orientation and dynamics in fluid flow (10–13).

Imaging is indubitably indispensable for cell analysis because images effectively convey certain messages about cells, such as cell size, shape, morphology, and distribution or location of labelled biomolecules within cells (14, 15). As cellular morphology analysis plays an important role in various biological studies and clinical diagnoses, such as cancer screening, conventional flow cytometry is much anticipated to incorporate imaging capabilities (16–18). Increasing flow cytometry's spatial resolution is to provide high-speed comprehensive analysis and in-depth imagery of every individual cell. In addition, some erroneous results yielded in conventional flow cytometry can be eliminated by acquiring and analysing the cell images to, for example, distinguish between cells, debris, and clusters of cells.

In contrast to pure quantitative measurements provided by conventional flow cytometry, the technique invented in seventeenth century—microscopy allows capturing

cell images that contains a wealth of information about a cell. While conventional flow cytometry measures forward scattered light to estimate relative cell size, microscopy yields exact cell size by its brightfield image. Advances of microscopy technique has realized both 3-dimensional and super resolution that allows imaging biological structure and function beyond the diffraction limit, producing extraordinarily detailed fluorescent cell images, but it can take as long as several minutes to produce such high-content images. Automated microscopy coupled with automated image analysis can be relatively fast with a typical throughput of several hundreds of cells per second. The technology called laser scanning cytometry (LSC) allows automated high-throughput image analysis to identify and measure cell properties with multiple spectra and high spatial resolution for measuring dynamic processes (19–24). Although LSC and high-throughput microscopy are suitable for studying complex biological pathway in a time-lapse manner, it is designed to work only with adherent cells. There are also some bottlenecks for high-throughput microscope systems, including mechanical stability when motorized stages and autofocus drive are required, image analysis problems caused by non-uniform illumination and cell-to-cell unmixing, sample and liquid handling (25), and above all, low throughput and yield in cell sorting. On the other hand, the development in mobile devices, especially in cell-phone cameras, has facilitated several cost-effective and field-portable imaging technologies, including lens-free optofluidic microscopy and cell-phone-based optofluidic fluorescent imaging cytometry (26, 27). Those miniaturizing and automating lab-on-a-chip platforms provide commendable image quality and even three-dimensional cell representations in some examples (28, 29). Yet those systems are most suitable for a relatively small sample volume and cannot match the high-throughput of conventional flow cytometers.

A parallel microfluidic cytometer (PMC) has been implemented to compromise between high-throughput and high-content, but has very limited 1-dimensional spatial resolution to resolve many sub-cellular components and structures compared to 2-dimensional cell images (30, 31). Recent advances in imaging technologies, electronics, and digital computing have enabled imaging flow cytometry (IFC) (32, 33). As an integration of fluorescence microscopy and conventional flow cytometry, IFC combines flow cytometry's single-cell identification and high-throughput with microscopy's cell image acquisition. Therefore, it becomes an ideal approach to simultaneously fulfil both analysis of morphological characteristics and phenotypic characterization of single cells within an enormous and heterogeneous population (34). Also, as the interest in performing IFC systems grows, the necessity of combining this technique with cell sorting becomes evident (35–38).

The basic idea behind IFC is scaling up flow cytometric spatial resolution to analyse more properties of cells. IFC aims at the fluidic-based platforms that have optical imaging functionality at informative spatial resolution while retaining the main features of conventional flow cytometry. The following section will describe recent IFC technologies and also those advances developed targeting at IFC, review their strengths and limitations.

1.3 Imaging Technologies for Flow Cytometry

Taking both high-throughput, i.e. high temporal resolution, and high spatial resolution into account, signal detection is the key challenge due to the fundamental trade-off between acquisition speed, sensitivity, and amount of information. Detectors used in imaging platforms can be divided to two types: 1) multi-pixelated imaging device, such as

charge-coupled device (CCD) and complementary metal-oxide-semiconductor (CMOS), and 2) single pixel photodetector, such as photomultiplier tube (PMT) and avalanche photodiode (APD). The rest of this section will discuss IFC platforms that employ these two types of detectors separately.

1.3.1 CCD/CMOS-based Detection Technologies

CCDs and CMOSs have a dense array of individual sensors in a 2-dimensional (2D) arrangement. Therefore, in an IFC system that uses CCD or CMOS as detector, by employing widefield illumination, 2D cell images can be produced as long as enough number of photons are sensed within a given exposure time by those individual sensors of such camera device placed at the image plane. The conundrum in this case is to increase the speed of such imaging tools. When applied in IFC that is on a cell-to-cell basis, the field of view is typically only 10's μm by 10's μm, so the large number of pixels in a CCD or CMOS camera are wisely re-arranged to work in parallel, either spatially or temporally.

The IFC developed by Millipore, e.g. ImageStream and FlowSight, relies on high-speed CCD cameras that use the time delay and integration (TDI) technique, which is originally designed to image objects moving along one axis at low light levels (32, 39, 40). This type of CCD provides higher sensitivity by having multiple rows of sensors which shift their partial measurements to the adjacent row synchronously with the motion of the moving cell image across the array of sensors. Applying this reading out technique, one can detect weak fluorescent signals without motion blur caused by increase in exposure time. The sensor arrays on CCD are divided into N columns to detect emission or scattered light of N different spectral ranges from cells. Using spectral decomposition elements, 12 images per cell can be acquired simultaneously. Figure 1.2 illustrates how the optics of

ImageStream/FlowSight works. Because the rich subcellular information acquired by ImageStream, various analysis and machine learning algorithms can be applied to study cell phenotype and subgroup classification.

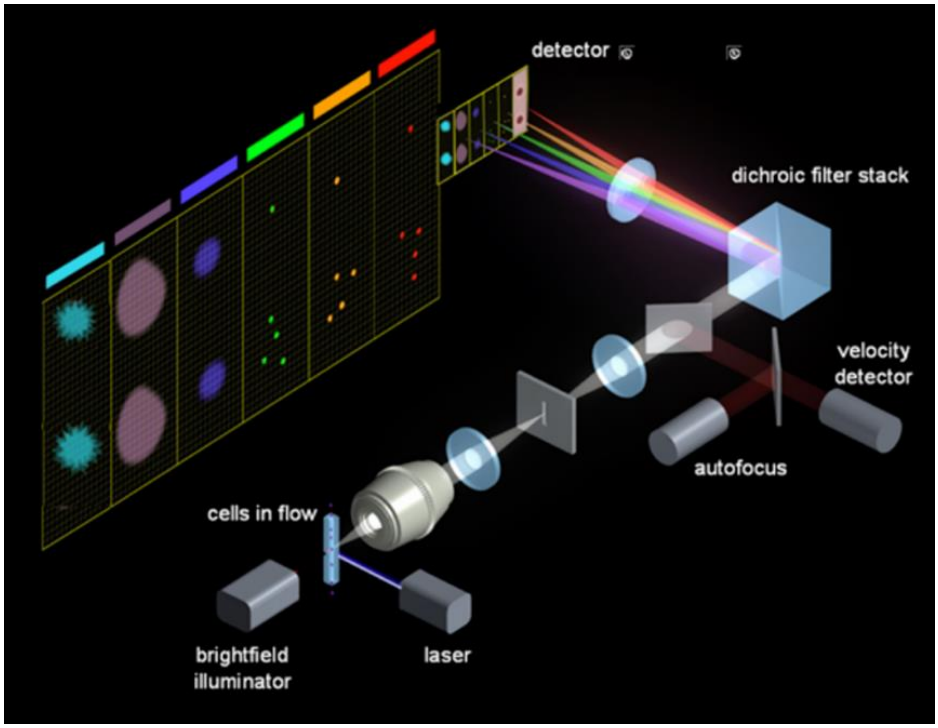

Figure 1.2 Optics of ImageStream

Because the translation of the cell is exactly synchronized with the vertical charge transfer of each pixel on the CCD, using the TDI reading out technique requires closely controlled fluidic system to ensure cells is centered and flow at a constant speed without rotation. This strict requirement hinders the system to adopt sorting mechanism, since any minor fluidic disturbance from downstream cell sorting can cause imaging instability. One limitation of the system speed is the inherent data downloading method of CCD: every unit sensor passively collects incoming photons and stores electrons till the whole line/array has been read out; accumulated charges are transferred from unit sensor to its neighbor

before they are dumped into the charge amplifier to be converted into voltage. This working scenario constrains the system's data access rate. On the other side, obtaining enough sensitivity without any gain like electron multiplication also prevents the system to reach higher throughput than 3,000 cells per second.

Instead of faster sophisticated photodetectors, a method named multi-field of view imaging flow cytometer (MIFC) was developed to image multiple changes simultaneously to obtain high-throughput. This method circumvents the trade-off between throughput and exposure time by projecting multiple fields of view onto the CMOS camera (41). The increase of throughput is, therefore, proportional to the degree of parallelization, i.e. number of parallel fluidic channels or number of isolated fields of view, while the cell flow velocity is kept at a moderate level. Due to microfabrication of multiple parallel microfluidic channels and on-top N × M microlens array, the total field of view has to be very wide to cover N × M channels. In the meanwhile, diffractive lens made of polydimethylsiloxane (PDMS) is used for its good monochromatic performance. Figure 1.3 shows the optical setup and the design of lens array.

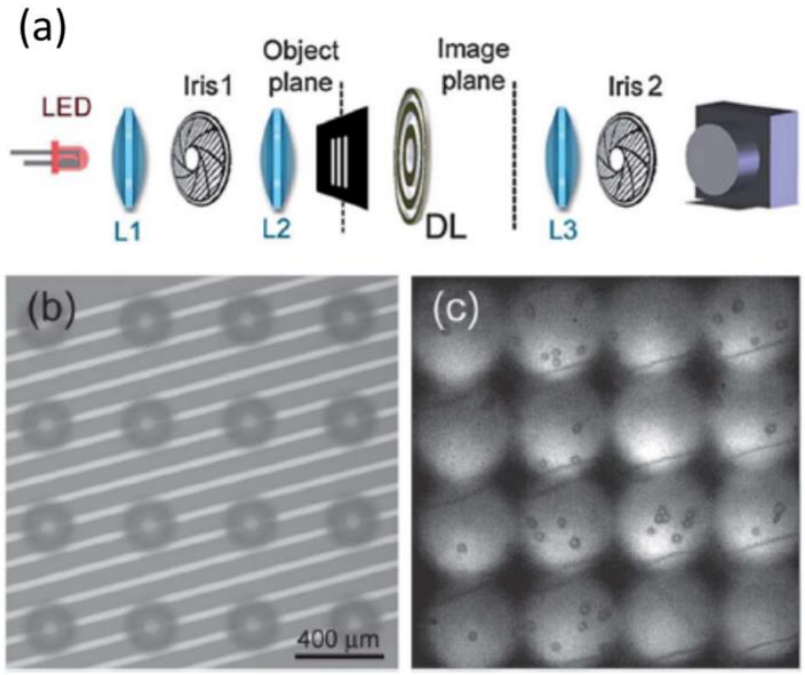

Figure 1.3 Multiple Field of View Imaging Flow Cytometer. (a) Diffractive lens wide field imaging system. L1 collimates the LED, L2 is a condenser that images Iris 1 onto the object plane. DL is the diffractive lens providing multiple field of view. L3 is a relay lens. (b) 16 object planes. (c) 16 imaging planes. Sample: 3.5um latex beads.

Despite that having more parallel fields of view means higher throughput, it is not always extendable due to field aberration caused by diffractive lens. While field aberration is relatively less severe in MIFC system since cells can be hydrodynamically focused and the field of view does not need to be significantly larger than single cells, typically 20 µm, chromatic aberration brought by diffractive lens makes MIFC work only in monochromatic mode. Light of various wavelengths has a various light path in an optical system that contains a diffractive lens. Its incompatibility with multi-mode and multi-spectral imaging becomes a hurdle of this IFC technique.

The primary way to image weak cell fluorescence signals in a CMOS-based system is to increase the exposure time, but consequential motion blur can dramatically downgrade the image quality. Motion blur occurs when the exposure time is longer than the time it takes the flowing cell to move a minimum resolvable distance. A technique that exploits temporally coded excitation effectively eliminates motion blur for fluorescence imaging of flowing cells (42). Instead of continuous illumination, a chopper wheel is used to generate modulated excitation pulse sequence with a pseudo-random code (shown in Figure 1.4). In this way, the captured images can be processed with known code sequence and known point spread function and finally be de-blurred using computational algorithms. Based on this technique, fluorescence image of cells moving faster than motion-blur velocity can be reconstructed. In addition, since the decoded image and moving velocity of the object is found computationally, the system can compensate for the effects of velocity variation in a laminar flow.

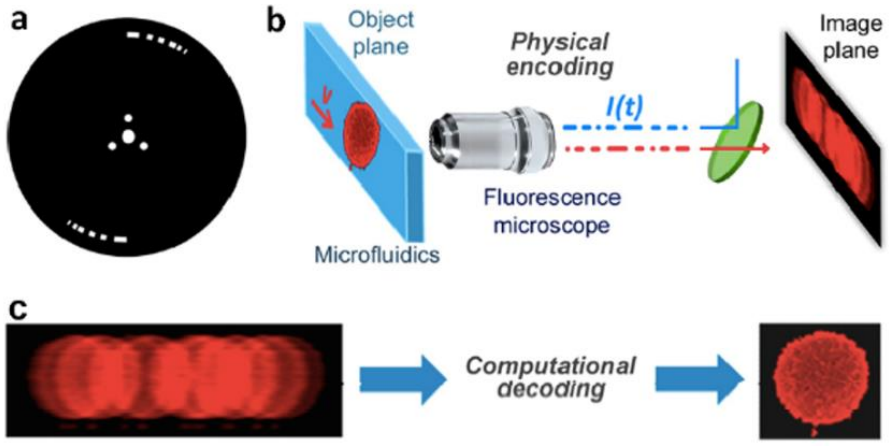

Figure 1.4 Coded excitation fluorescence microscope. (a) Chopper wheel that modulates the excitation beam with a pseudo-random code. (b) a microfluidic device imaged by 40X fluorescent imaging microscope. (c) Raw blur encoded images captured by the camera and decoded images after computational approach.

1.3.2 PMT-based Detection Technologies for IFC

PMTs have superb sensitivity at photon counter level and high dynamic range because of its internal tandem electron multiplication and gain adjustment. PMT also can provide higher bandwidth and lower dark noise than CCD/CMOS camera to support high-throughput IFC systems. However, the readout of single-pixel PMT presents the number of photons detected only in time domain, which contains no spatial information. In some high-speed microscopy laser scanning cytometry techniques, PMTs are combined with laser spot scanning to collect the entire light emitted or scattered by the illuminated cell and output a temporal signal. Cell images are then retrieved by assembling the intensity signal in time-domain according to the laser scanning position. Therefore, the overall throughput is limited by the speed of serial beam scanning. Instead of relying on mechanical beam scanning, several techniques have been developed to transfer spatial information to either frequency domain or time domain in order to make use of PMT's extra bandwidth that has not been fully utilized in conventional flow cytometers.

An ultrafast optical imaging modality named serial time-encoded amplified microscopy (STEAM), as shown in Figure 1.5, has been built for blur-free imaging of cells flowing at high speed (43–45). Different than the light sources, including light-emitting-diode (LED), laser, and mercury lamp, used in conventional flow cytometry or fluorescence microscopy, a mode-locked femtosecond pulse fiber laser is used to generate illuminating near-infrared light with wide spectral bandwidth of 10's nm centered at the ~1000 nm wavelength. The ultrafast broadband laser pulses are spectrally encoded by using an optical spatial disperser so that a 1D or 2D spectral rainbow for illumination is generated. In this way, the one-to-one spatial-to-spectral relation is obtained. In other

words, every individual point of the cell is illuminated by light at a specific wavelength. After being recombined by the spatial disperser and temporally stretched by a dispersive medium, typically a long optical fiber, the transmitted rainbow is detected by a single-pixel photodetector. The output temporal waveform, therefore, represents the spatial information encoded by the cells being illuminated. IFC based on time-stretching method can achieve throughput as high as 100,000 cells per second. In addition to one to one spatial-spectral mapping, encoding one location with multiple wavelengths is also available for more efficient measurements (46).

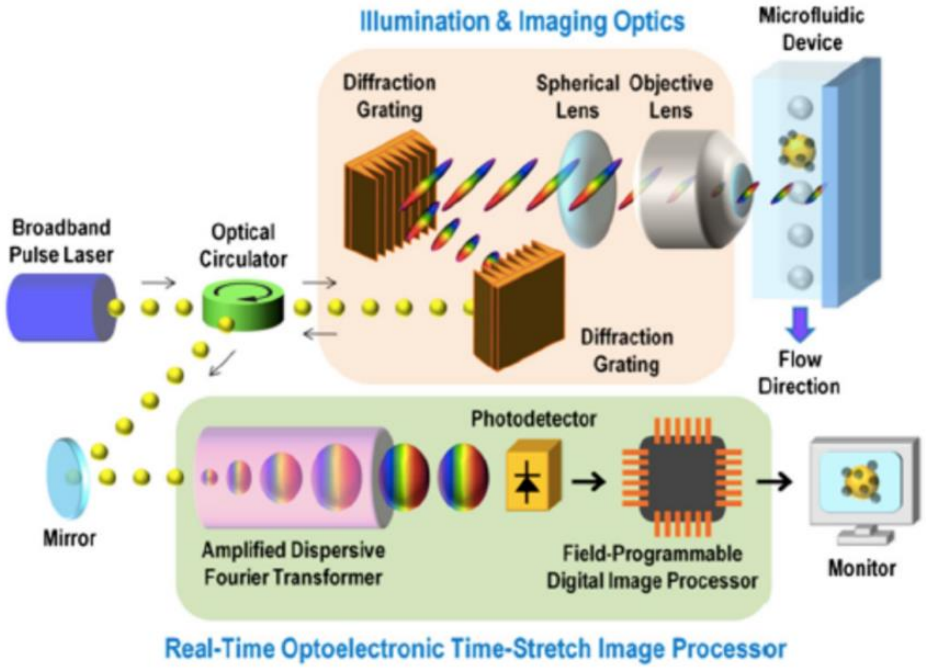

Figure 1.5 Schematic of the STEAM flow analyzer. Imaging and illumination optics take blur-free images by encoding object location information into spectral domain. ADFT converts spectral information into time domain through time-stretch method and processed by real-time imaging processor.

Besides producing brightfield imaging, the STEAM can produce phase-contrast images of cells by generating two 1D orthogonally-polarized spectral rainbow for illumination (47, 48). However, due to the high attenuation in visible spectral range of one key optical component applied in the time-stretching-based system—optical fiber and the incoherence of fluorescence, this technology has not been able to produce fluorescence imaging, which is an essential function in numerous applications of cell analysis. Incorporating 1D fluorescence detections by employing additional lasers enables the system to retain features of conventional flow cytometry, but such fluorescence signals do not benefit from the time-stretching technique (49, 50). Another bottleneck of this technique, also due to the limited working spectral range to near-infrared regime (i.e. around 1000 nm), is that the spatial resolution does not go beyond the wavelength related diffraction limit.

Adopting the schemes in radiofrequency communications, an emerging technique named fluorescence imaging using radiofrequency-tagged emission (FIRE) has made high-speed fluorescence imaging possible (51, 52). As shown in Figure 1.6, the continuous-wave laser is converted to multiple intensity-modulated excitation beams by using an acousto-optic deflector (AOD) and an acousto-optic frequency shifter (AOFS) in the optical setup. Every individual point of the cell within the imaging field of view is excited by the light modulated at a distinct radio frequency. Acousto-optic components diffract light to different angle in 1D, and cells are moving at a certain speed along the orthogonal direction to the acousto-optically scanned beam in an IFC system. Thus, each pixel in a 2D cell image captured by FIRE is represented by a unique combination of one radiofrequency and one time-point. The resulting throughput is up to 50,000 cells per second. In addition,

by increasing the bandwidth from that of employed AOD, the speed of this imaging technique is further exploited to be limited by fluorescence lifetime (53).

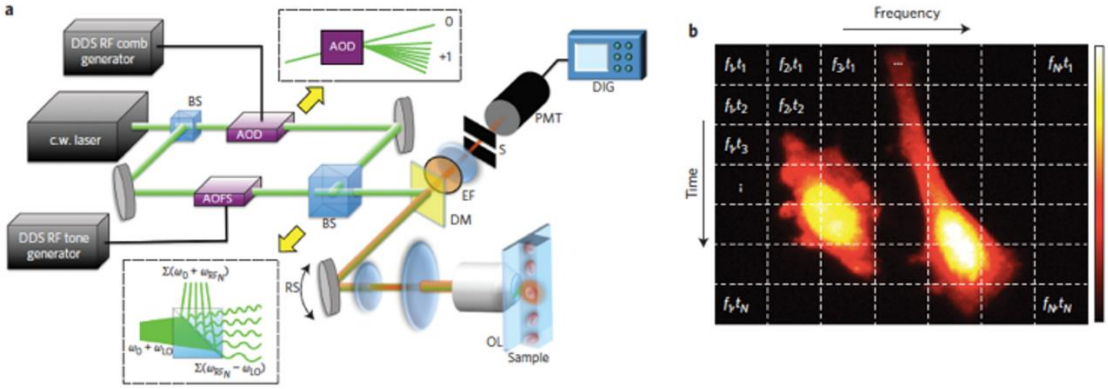

Figure 1.6 FIRE microscopy. **(a)** Schematic diagram of the FIRE microscope. Upper inset: the AOD produces a single diffracted first-order beam for each radiofrequency comb frequency. Lower inset: beat frequency generation at the MZI output. **(b)** Gabor lattice diagram of FIRE's frequency-domain multiplexing approach. Points in same horizontal line are excited in parallel at distinct radiofrequencies. The horizontal line is scanned by a galvo-mirror to acquire a 2D image.

Because the time-domain signal from a FIRE system is a Fourier superposition of the radiofrequency-tagged emission from one row of pixels, Fourier transform is required in data processing. This can make the system difficult to realize real-time processing and instant result generation. Besides, the operations of the key components in a FIRE system—AOD and AOFS—are wavelength-dependent, which makes multicolor imaging very challenging. In addition, because this radiofrequency tagging technique is only applied to coherent light source, the FIRE system is not suitable for bright-field imaging where an LED source is preferred to avoided speckle noise and interference.

1.4 Scope of Dissertation

This dissertation covers the invention and development of the two-dimensional (2D) and the three-dimensional (3D) imaging technologies for flow cytometry.

Earlier in Chapter 1, we introduce some background about IFC, and then review multiple imaging techniques for flow cytometry.

Chapter 2 presents the development of the high-throughput 2D imaging flow cytometry system based on the novel spatial-temporal transformation technology. This technology uses mathematical algorithms and a specially designed spatial filter to give flow cytometers capabilities of high-throughput, motion-blur-free, multi-color, and multi-mode imaging of single cells.

Chapter 3 moves forward to develop the high-throughput 3D imaging flow cytometry system for biological applications. We combine orthogonal light-sheet scanning illumination with the previous spatial-temporal transformation detection to produce 3D cell image reconstruction from a cameraless single-pixel photodetector readout.

In the end, Chapter 4 summarizes this dissertation and briefly discusses several future directions.

Chapter 1, in part, is a reprint of the material as it appears in Lab on a Chip 2016. Y. Han, Y. Gu, A. C. Zhang, and Y.-H. Lo, "Review: imaging technologies for flow cytometry". The dissertation author was the first author of this paper.

Chapter 2

Imaging Flow Cytometry Using Spatial-Temporal Transformation

Flow cytometry analyses multiple physical characteristics of a large population of single cells as cells flow in a fluid stream through an excitation light beam. Flow cytometers measure fluorescence and light scattering from which information about the biological and physical properties of individual cells are obtained. Although flow cytometers have massive statistical power due to their single cell resolution and high throughput, they produce no information about cell morphology or spatial resolution offered by microscopy, which is a much-wanted feature missing in almost all flow cytometers. In this paper, we invent a method of spatial-temporal transformation to provide flow cytometers with cell imaging capabilities. The method uses mathematical algorithms and a specially designed spatial filter as the only hardware needed to give flow cytometers imaging capabilities. Instead of CCDs or any megapixel cameras found in any imaging systems, we obtain high quality image of fast-moving cells in a flow cytometer using photomultiplier tube (PMT) detectors, thus obtaining high throughput in manners fully compatible with existing cytometers. In fact, our approach can be applied to retrofit traditional flow cytometers to

become imaging flow cytometers at a minimum cost. To prove the concept, we demonstrate cell imaging for cells travelling at a velocity of 0.2 m/s in a microfluidic channel, corresponding to a throughput of approximately 1,000 cells per second.

2.1 Introduction

Cell imaging and high throughput single cell analysis are the primary techniques for studies of cell and molecular biology and medicine (5, 54). Microscopy, which is by far the most important imaging tool in biology and medicine, has capabilities to generate cell images of extraordinary details, such as fluorescent images from specific macromolecules, organelles, or subunits of the cells . Yet a microscope yields information via imaging at a relatively low throughput (55). Given the heterogeneous properties of biological objects such as cancer cells and cells going through different stage of life cycles, much improved understanding of cell and tissue properties can be achieved from the individual properties of a very large population (thousands to millions) of cells. The limited throughput of microscopy techniques has become an impediment for studies of the heterogeneous characteristics of biological samples. On the other hand, flow cytometry is a powerful tool supporting very high throughput analysis, enabling detection of single cell properties at rates from hundreds of cells per second to over 100,000 cells per second (3). Flow cytometers can measure and analyze multiple physical parameters of cells, including a cell's relative size, nuclear granularity, and fluorescence from specific markers or constituents, as each cell in a fluid stream flows through a region of optical interrogation area illuminated by laser beams. However, conventional flow cytometers do not produce the spatial resolution as microscopy does to allow detailed investigation of cell properties

that are needed in many applications. As an analogy, flow cytometers can quickly tell male from female over a large group of people without being able to recognize the facial features of each individual, whereas imaging cytometers can reveal the detailed facial features of each person but cannot perform the function fast enough to a large number of people that need to be investigated.

In spite of the above constraint, flow cytometers have been extensively used in biomedical research and playing an increasing role in clinics because of their advantage of high throughput, single cell resolution, and compatibility with cell sorting capabilities (35, 45). However, the lack of high spatial resolution that contains valuable phenotypical and morphological information crucial to diagnosis and cell analysis provides a strong incentive to incorporate imaging capabilities into flow cytometry (10, 51, 56). The recently invented parallel microfluidic flow cytometer uses six-pixel one-dimensional spatial information to investigate nuclear translocations, but has very limited spatial resolution to resolve many other sub-cellular compartments and structures compared to a two-dimensional image (30, 31). To date the only successful effort in this area is the imaging flow cytometer developed by Amnis/Millipore (e.g. ImageStream) (15, 57). Significantly different from all other flow cytometers, the Amnis flow cytometer relies on the time delay and integration (TDI) high-speed charge-coupled device (CCD) camera with a large number of pixels, as opposed to photomultiplier tubes (PMTs) used in almost all today's flow cytometers to take advantage of PMT's high speed and superb sensitivity (32). The Amnis system is much more costly than conventional flow cytometers, and is not ready for integration of cell sorting capabilities due to its unique operation requirements and optics design. As a result, only a very small number (<5%) of flow cytometers deployed today

has acquired the imaging capabilities in spite of the strong desire for such attractive features in flow cytometers (39, 58).

In this paper we demonstrate a spatial-to-temporal transformation technique to unify the design of flow cytometer and imaging cytometer. Our design is fundamentally different from the CCD- or CMOS-based technology adopted by nearly all imaging systems today, which requires a relatively long integration time (or exposure time) to capture pictures frame by frame and therefore has speed limitation for imaging cells travelling at high speed (59). Rather than using any megapixel imaging devices, we use a specially designed spatial filter placed in front of the PMT detector in the flow cytometer to produce a temporal waveform of the fluorescent or scattering signal. This waveform, encoded by the spatial filter, contains all the information needed to map out the spatial distribution of the signal of a cell, thus allowing construction of the cell image from the temporal waveform. The design is compatible with the existing optic design of conventional flow cytometers, and can be easily implemented to upgrade a conventional flow cytometer to become one with cell imaging capabilities at minimum cost (60). To prove the concept, we show single cell images of A549 human lung adenocarcinoma epithelial cells in a flow cytometer prototype shown in Figure 1a. The flow speed of the cells is 0.2 m/s, corresponding to a throughput of approximately 1,000 cells per second.

2.2 Methods

2.2.1 Experimental Setup of the Imaging Flow Cytometer

A diagram of the imaging flow cytometer (IFC) prototype is shown in Figure 2.1. The system consists of three main units: 1) fluidic system for introducing cells into a

microfluidic channel, 2) optical system for illumination and detection of the light signals, 3) electronic system for data acquisition and processing. Except for the spatial filter detailed in Figure 2.1b, all other parts are common to any conventional, generic flow cytometers, so the results obtained here can be generalized to other flow cytometers with only minor modifications.

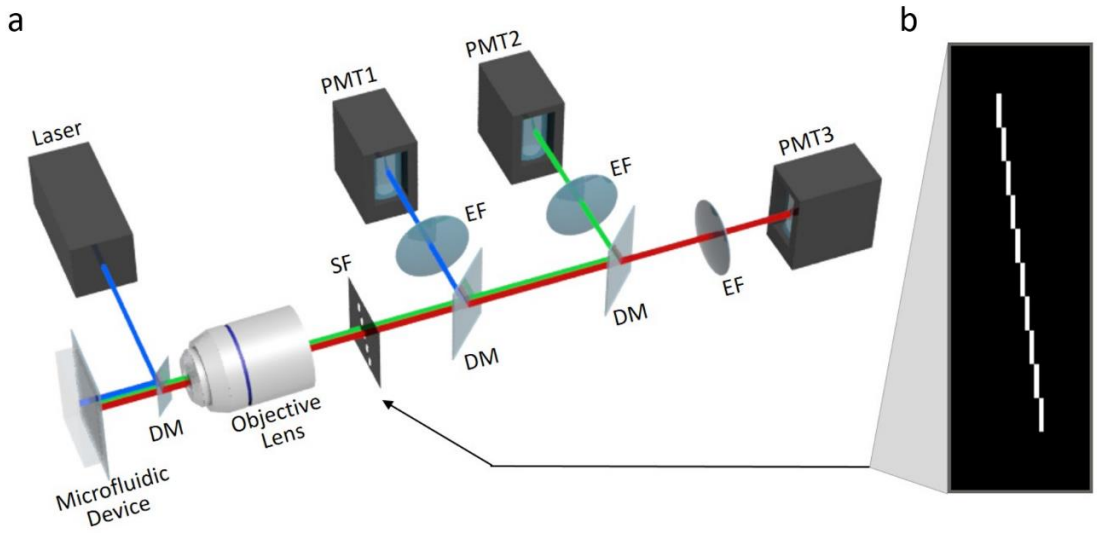

Figure 2.1 Implementation of imaging flow cytometer. (a) Schematic diagram of the imaging flow cytometer system. DM, dichroic mirror; SF, spatial filter; EF, emission filter; PMT, photomultiplier tube. (b) Spatial filter design that has ten 100 μm by 1 mm slits positioned apart in the way of one is immediately after another in both x-direction and y-direction

At first the suspended cells are introduced into the microfluidic channel and hydrodynamically focused by sheath flow, ensuring that the cells travel in the center of the fluidic channel at a uniform velocity (61). The fluorescence emission and backscattering light from the sample are detected by two individual PMTs in a wide-field fluorescence microscope configuration. Here cells are flown in a microfluidic channel made of soft-molded PDMS bonded to a glass substrate. To accommodate the geometry of the

microfluidic device, the laser beam is introduced to the optical interrogation site in the fluidic channel by a miniature 45-degree dichroic mirror positioned in front of a 50X objective lens (NA=0.55, working distance=13 mm). The size of the 45-degree dichroic mirror is small enough to allow the backscattering light (147° to 168° with respect to the normal incident light) to pass the dichroic mirror and enter the objective lens. A spatial filter having the pattern shown in Figure 2.2b is inserted in the detection path right at the image plane of the optic system. Both the fluorescent and backscattering light from a travelling cell are collected by the objective lens and pass the filter before reaching their respective PMT detectors. Another dichroic mirror splits the light by its spectrum to route the desired emission bands to the appropriate PMTs. Finally, the output of each PMT is sent to a computer and processed to generate cell images from fluorescence and back scattering. Although the system in Figure 2.1 shows only one PMT for detection of fluorescent signal, it is straightforward to add more PMTs and, if necessary, more excitation laser beams, to produce multi-color fluorescent signals as in any conventional flow cytometers.

2.2.2 Cell Image Reconstruction Algorithm

The concept of spatial-to-temporal transformation can be mathematically formulated in the following:

$$S(t) = \int_{x,y} Cell(x, y - Mvt) \cdot F(x, y) \cdot I(x, y) dxdy \qquad \text{Eq. 2-1}$$

, where $S(t)$ is the measured PMT signal, $Cell$ is the two-dimensional cell fluorescence or scattering intensity profile, $F(x, y)$ is the characteristic function of the spatial filter, $I(x, y)$ is the intensity profile of laser illumination, y is along the cell travelling direction and x is

along the transverse direction, and M is the magnification factor of the optical system pertaining to the flow cytometer. As the cell travels in the microfluidic channel at a speed v, the image projected onto the spatial filter travels at an effective speed of Mv. To simplify the mathematical process of solving for $Cell$ in Equation 2-1, here we choose $F(x,y)$ to be a series of rectangle function represented in Equation 2-3 and $I(x,y)$ to be a constant from a laser beam of uniform intensity.

$$F(x,y) = \sum_{x=1}^{N} \big(u(y-(x-1)L) - u(y-xL)\big) \qquad \text{Eq. 2-2}$$

, where $x = 1, 2, \dots, N$ is the number of rows in the spatial filter, L is the length of the rectangular slit that transmits fluorescent or scattering light. We can rewrite Equation 2-1 as

$$S(t) = \sum_{x=1}^{N} \int_{y} Cell(x, y-Mvt) \cdot \big(u(y-(x-1)L) - u(y-xL)\big)dy \qquad \text{Eq. 2-3}$$

We can solve for "$Cell$" by taking the time derivative of Equation 2-3.

$$\frac{d}{dt}S(t) = \sum_{x=1}^{N} \frac{d}{dt} \int_{-\infty}^{\infty} Cell(x, y-Mvt) \cdot \big(u(y-(x-1)L) - u(y-xL)\big)dy \qquad \text{Eq. 2-4}$$

Assuming the cell orientation does not change within such a short time interval, one can represent Equation 2-4 as the following:

$$\frac{d}{dt}S(t) = \sum_{x=1}^{N}\int_{-\infty}^{\infty} Cell(x,y')$$

$$\cdot\frac{d}{dt}\big(u(y'+Mvt-(x-1)L)-u(y'+Mvt-xL)\big)dy'$$

$$= \sum_{x=1}^{N}\int_{-\infty}^{\infty} Cell(x,y') \qquad \text{Eq. 2-5}$$

$$\cdot Mv\big(\delta(y'+Mvt-(x-1)L)-\delta(y'+Mvt-xL)\big)dy'$$

$$= \sum_{x=1}^{N} Cell(x, Mvt-(x-1)L) - \sum_{x=1}^{N} Cell(x, Mvt-xL)$$

To obtain Equation 2-5, we have used $y' = y - Mvt$. When the cell size does not exceed the slit length L, within the specific time interval $t \in \left((x_0-1)\frac{L}{Mv}, x_0\frac{L}{Mv}\right)$, $\frac{d}{dt}S_{x_0}(t) = Cell_{x_0}(y) - Cell_{x_0-1}(y)$. As a result, the cell image can be constructed from the following relation:

$$Cell_{x_0}(y) = \frac{d}{dt}S_{x_0}(t) + Cell_{x_0-1}(y) \qquad 1 \le x_0 \le N \qquad \text{Eq. 2-6}$$

Generally, with the spatial filter described above inserted at the image plane, fluorescence from different parts of the cell will pass different slits at different times. As a result, the waveform of the fluorescent signal from the PMT consists of a sequence of patterns separated in time domain, and each section of the signal in the time domain corresponds to the fluorescent signal generated by each particular segment of the cell. After the light intensity profile over each slit is received, the cell image of the entire cell can be constructed by splicing all the profile together. In our prototype, the spatial filter contains

ten 100 μm by 1 mm rectangular slits positioned in sequence as shown in Figure 1b. An alternative spatial filter that has two slits of 100 μm by 1 mm in x- and y-direction, respectively, in front of the slit tandem can be applied for precise calculation of cell traveling speed for each cell. With a 50X objective lens (M = 50) in our prototype, the filter design allows us to construct the fluorescent or scattering image of a travelling cell no larger than 20 μm by 20 μm using the algorithm described in Equation 2-6, which requires a minimum amount of computations and is suitable for high-throughput, real-time image-based cell classification and sorting.

2.2.3 Microfluidic Device Fabrication

The microfluidic device (as shown in Figure 2.2) consists of a glass substrate and a piece of PDMS with microfluidic channel. It has three inlet channels and a 250 μm wide main channel to allow a single stream of suspended single cells hydrodynamically focused by sheath flow.

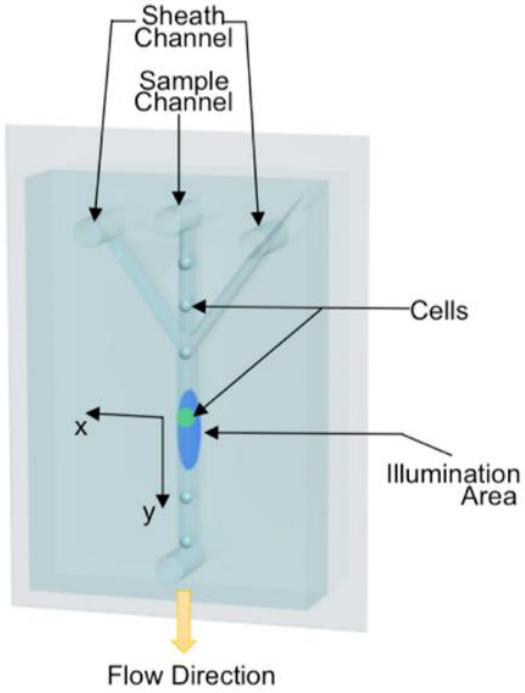

Figure 2.2 Microfluidic device in IFC. Suspended cells are controlled by sheath flow to travel in the center of the microfluidic channel at a uniform velocity.

The microfluidic device was fabricated using the standard polydimethylsiloxane (PDMS) replica molding methods. The Si mold masters were fabricated by the reactive ion etching (RIE) process. The microfluidic channels were drawn in AutoCAD (Autodesk, Inc.), and were photolithographically defined using negative photoresist (NR9-1500PY, Futurrex, Inc.), which serves as an etch mask during the following dry-etching process. A 4-inch silicon wafer was etched at room temperature using inductively coupled plasma (ICP) reactive ion etching (ICP RIE; Plasmalab 100, Oxford Instruments) to reach a depth of 75 μm. Plasma ignited from a mixture of O_2 and SF_6 gases performed the etching and sidewall passivation, resulting in smooth and vertical channel walls. The Si mold master was silanized by vapor deposition of trichlorosilane (TCI Inc.) to facilitate PDMS de-

molding. A replica was made by casting the PDMS (Sylgard 184, Dow Corning), mixed in the standard 10:1 ratio of base to curing agent, over the Si mold master. After thermal curing in the oven for 3 hours at 65 °C, the PDMS layer was peeled off of the mold, and holes for inlets and outlets were punched. The surfaces of the demolded PDMS layer and a glass wafer were both treated with UV/Ozone to facilitate covalent bonding of them to form microfluidic channels for the imaging flow cytometer experiment.

2.2.4 Optical System

A 25 mW 488-nm single-mode fiber coupled laser (FTEC2, Blue Sky Research) has a circular beam shape with Gaussian energy distribution. A top-hat beam shaper (Osela, Inc.) is used to convert the Gaussian beam to a uniform top-hat profile, which illuminates an area of 100 μm (x-direction) by 350 μm (y-direction). The fluorescence passing the miniature dichroic mirror with 500 nm cut-off wavelength (ThorLabs) and the scattering light are collected through a 50X/0.55 objective lens (Mituyoyo). The light intensity signal in each channel is acquired by a PMT (H9307-02, Hamamatsu) and recorded using LabVIEW. The saved raw data are processed in MATLAB implementing the aforementioned algorithm.

2.2.5 Spatial Filter Fabrication

The design of spatial filter was drawn in AutoCAD and printed to a transparency mask at 20,000 dots per inch (dpi). A layer of negative photoresist (NR9-1500PY, Futurrex, Inc.) was spun at 3,000 rotations per minute (rpm) on a 6-inch glass wafer. The wafer was heated on a hot plate at 150 °C for 3 minutes then exposed to UV light (EVG620NT, EV Group) through the transparency mask. Post UV exposure, the wafer was baked at 100 °C

for another 3 minutes before development in RD6 (Futurrex, Inc.) for 12 seconds. A film of 200 nm thick aluminum was sputtered onto the glass wafer. After metal lift-off, the patterns of the spatial filter were formed and the glass wafer was diced into 15 mm by 15 mm pieces. To help hold the spatial filter in the flow cytometer system, the spatial filter having ten 1 mm by 100 μm slits was mounted to a sample holder fabricated by 3D printing method.

2.2.6 Preparation of Cell Samples

The A549 human lung adenocarcinoma epithelial cell samples were harvested from culture and labelled with CellTrace CFSE Cell Proliferation Kit (Life technologies) that has excitation and emission peaks at approximately 492 nm and 517 nm, respectively. After incubation in 4% formaldehyde for 20 min, the A549 cells were washed and resuspended in phosphate buffered saline (PBS). Before every imaging experiment, the suspension was diluted in PBS to a concentration of 200 cells/μl. The MDA-MB-231 human breast cancer cell samples were cultured to 80% confluency in 100 mm dish. 80 μL of 100x dilution of the stock solution of 1.0 μm, 2% solids TransFluoSpheres Carboxylate-Modified Microspheres (Life technologies) that has excitation and emission peaks at approximately 488 nm and 645 nm, respectively, was added to the cell culturing plate. After 10-hour incubation, the MDA-MB-231 cells were harvested and labeled with CFSE kit. To arrest A549 cells at the G1 phase, Mitomycin (10 μg/ml) dissolved in DMEM, mixed with 0.5% FBS and 1% PS, was added to the culture medium and then the cells were incubated for 3 hours prior to the experiment. To arrest cells at the G2/M phase, 50 ng/ml of nocodazole in DMEM, mixed with 0.5% FBS and 1% PS, was added to the culture medium and the cells were cultured for 16 hours. Cells arrested at the designed phase were washed with

PBS and suspended in 4% formaldehyde. After keeping the cell suspension at room temperature for 20 minutes, the sample was centrifuged at 1000 rpm for 10 min and the supernatant of cell suspension was carefully discarded. After washing the sample left in the tube with PBS, the fixed cells were resuspended in PBS to the concentration of 200 cells/μL.

2.2.7 Measurements of Cell Morphological Features

The output images from the imaging flow cytometer represent a 20 μm by 20 μm area; the cell fluorescence images from the fluorescence microscope (BZ-9000, Keyence) are also cropped to the same area. To measure the morphological features of both the cell images reconstructed by the imaging flow cytometer and taken by the fluorescence microscope, all images are processed using ImageJ. Two image sequences that include 100 images from each system are imported to ImageJ. After setting the measurements to include area and shape descriptors, the command "Analyze Particles" is used to measure the concurrently thresholded images. The mean values and the standard deviations in Table 1 are calculated based on the results from ImageJ. For the Feret's Diameter measurements of backscattering images, 300 images from each of the G1 arrested cells and the G2/M arrested cells are analyzed using the same method in ImageJ. To avoid multiple measurements in one image due to the disconnected patterns, especially in the backscattering images of G2/M arrested cells, all the images, including both G1 and G2/M cell images, are smoothed twice and concurrently thresholded, and only the largest Feret's Diameter in every image is recorded.

2.3 Results

2.3.1 Image Reconstruction of Simulated and Experimental Signal

To demonstrate the feasibility of this approach by simulation, we use a cell image as the cell under test and have the cell travel through an illumination beam spot at a speed of 0.24 m/s. The fluorescence light that passes the slits on the spatial filter is sampled at a rate of 500 kHz. Figure 2.3a shows the original cell image, the time-domain output signal through the spatial filter, and the reconstructed cell image using the aforementioned algorithm. Compared to the original cell image, the reconstructed image from simulation shows identical features.

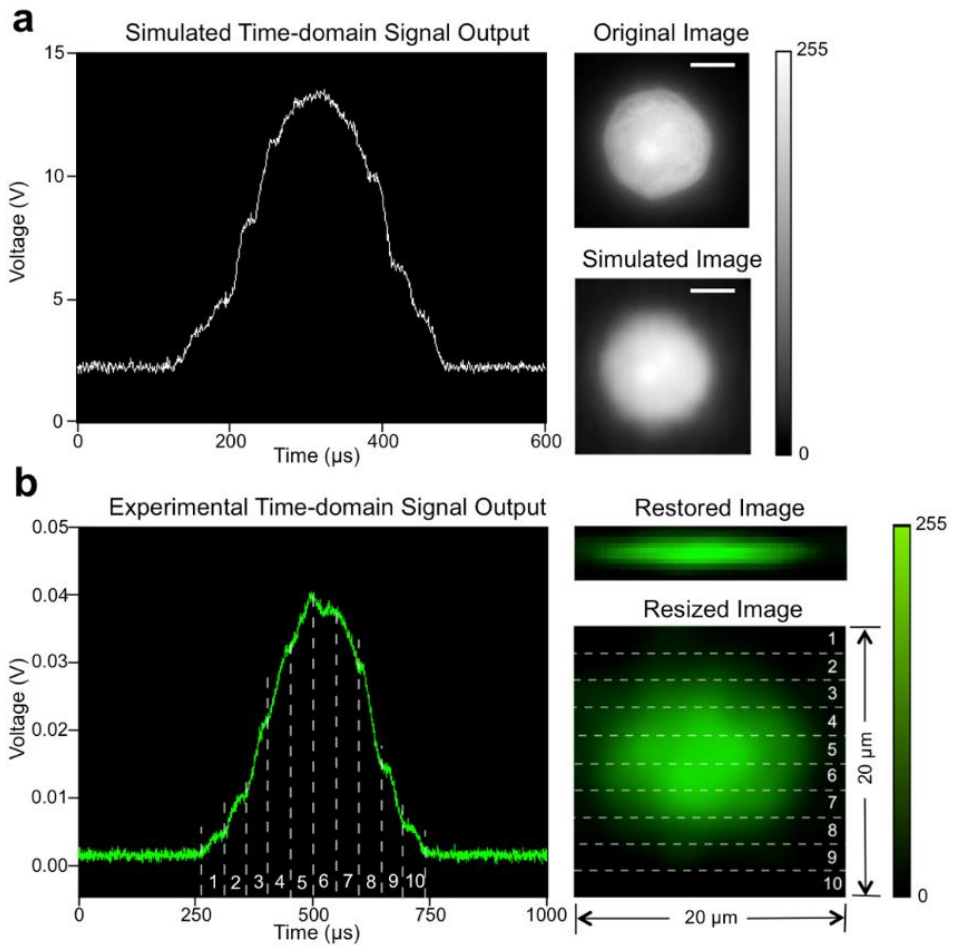

Figure 2.3 Illustration of restoring cell images from PMT signals. (a) Simulation result: result of time-domain light intensity signal from simulation, original cell image used as input for simulation, and corresponding restored image. Scale bar is 5 μm. (b) Experimental result: time-domain PMT output signal of fluorescent light from an A549 cell stained with CellTrace CFSE, corresponding original fluorescence image restored by algorithm, and corresponding resized fluorescence image to show the real size of the cell. The numbered regions segmented by dashed lines demonstrate the correspondence between the time-domain signal and the resulting image. Size is labeled in figure.

During every experiment, once the cells are injected into the microfluidic channel, a two-slit filter is inserted at the image plane to determine the cell travelling velocity, followed by applying the aforementioned spatial filter. The time-domain signal for each

cell is captured by thresholding the PMT readout. Figure 2.3b shows the experimental result of a typical PMT signal and the fluorescence cell image constructed from the PMT signal using Equation 2-6. The spatial resolution of the reconstructed image in x- (transverse) direction depends on the number of the slits on the spatial filter, and in y- (cell travelling) direction depends on the sampling rate and cell flow rate. In the original image reconstructed by the imaging flow cytometer (shown in Figure 2.3b), the effective pixel size is 2 μm in x-direction and about 0.4 μm in y-direction. The recovered image is then resized to 80 by 80 pixels to better represents a 20 μm by 20 μm area in the object plane in the microfluidic channel. Using a 50X/0.55NA objective lens, 500 kHz sampling rate for acquiring PMT signal, and 0.2 m/s cell travelling speed that is given by 12 μL/min sample flow rate and 120 μL/min sheath flow rate, the effective size of the pixel in y-direction is $\frac{L}{(L/Mv)\times R} = \frac{Mv}{R} = 0.4$ μm which is smaller than the Rayleigh Criterion, thus resulting in a diffraction-limited resolution in y-direction. Here R is the sampling rate of PMT readout in this calculation.

2.3.2 Fluorescent Cell Images Captured by the IFC System

Figure 2.4a shows representative fluorescence images of fluorescently labeled A549 cells flown at 0.2 m/s in a microfluidic channel, producing a throughput of around 1,000 cells/s. For comparison, Figure 2.4b shows images of the stationary fluorescently labeled A549 cells between a glass slide and a coverslip captured by a fluorescent microscope with a CCD camera under at least 50 ms exposure time; Figure 2.4c shows images from same batch by a confocal microscope. The resulting images from the imaging flow cytometer appear to be similar to the images of still cells from a fluorescence

microscope, even though in the imaging flow cytometer, the cells are travelling at a speed of 0.2 m/s and the signals that give rise to the cell images are detected by a single PMT in a setup and configuration compatible with conventional flow cytometers.

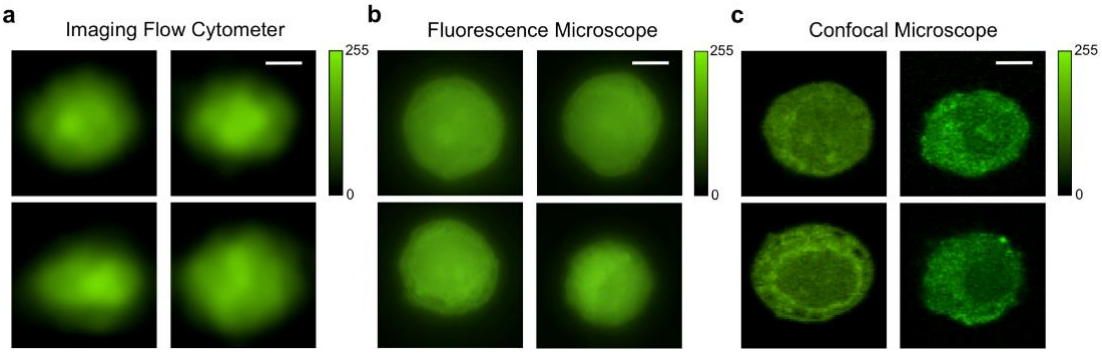

Figure 2.4 Comparison of spatial-filter-based flow cytometry imaging and wide-field fluorescent imaging. All images are of A549 human lung adenocarcinoma epithelial cells, stained with CellTrace CFSE. (a) Representative imaging flow cytometer reconstructed fluorescence images of cells flowing at a velocity of 0.2 m/s. Objective lens: 50X/0.55 (b) Representative wide-field fluorescence images of stationary A549 cells taken by fluorescence microscope. Objective lens: 100X/0.90. (c) Representative confocal microscope images of stationary A549 cells. Objective lens: 63X/1.30. Size of all image crops is 20 μm by 20 μm; scale bar is 5 μm.

Table 2-1 shows comparisons in size and shape descriptors of cell images acquired by our imaging flow cytometer prototype and fluorescence microscope. The following measurements are included: Area is the above-background area of the cell image; circularity equals to $4\pi A/P^2$; P is perimeter of the cell image; solidity is the ratio of area to convex area; aspect ratio is the ratio of major axis to minor axis of the cell image's fitted ellipse. Based on 100 cell fluorescence images randomly picked from each group, the measured cell size, circularity, and solidity of the images reconstructed by the imaging flow cytometer are highly consistent with the images taken by the fluorescence microscope, with exception of the aspect ratio defined as the ratio of the major axis to the minor axis of

the fitted ellipse. The appreciable difference in the cell aspect ratio between the imaging flow cytometer and fluorescent microscopy is attributed to cell deformation by the fluidic dynamic shear stress, carrying information about cell stiffness, a property of biological significance.

Table 2.1 Comparison of cell morphological features between fluorescence images reconstructed by the 2D imaging flow cytometer prototype and taken by fluorescence microscope based on 100 cell images from each group.

Cell Images from	Area (um^2)		Circularity		Solidity		Aspect Ratio	
	Mean	St. D.	Mean	St. D.	Mean	St. D.	Mean	St. D.
Imaging Flow Cytometer	126.77	3.199	0.82	0.028	0.96	0.007	1.52	0.088
Fluorescence Microscope	128.74	4.511	0.87	0.048	0.96	0.013	1.08	0.064

2.3.3 Cells and Beads Imaged by the IFC System

The imaging flow cytometer system enables fast fluorescence imaging using only a single PMT instead of pixelated CCD. Figure 2.5 shows representative two-color fluorescence images of fluorescently labeled MDA-MB-231 human breast cancer cells bond with fluorescent microbeads; the cells are flowing in the microfluidic channel at 0.25 m/s.

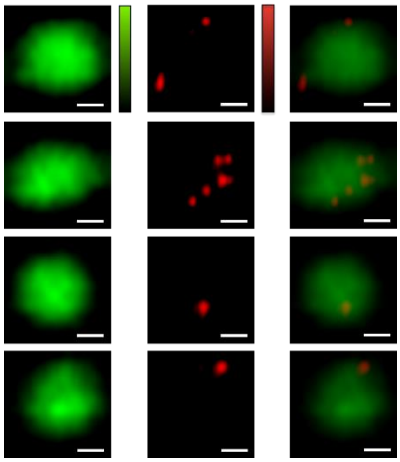

Figure 2.5 Representative two-color fluorescent images. All images are of MDA-MB-231 human breast cancer cells stained with CellTrace CFSE, cell membrane bond with 1 μm fluorescent beads, flowing in the microfluidic channel at 0.25 m/s. Scale bar is 5 μm.

2.3.4 Backscattering Image Captured by the IFC system

Our spatial-temporal transformation technique is not restricted to specific modes of signals. In the following we show that the approach is capable of combining fluorescence images with backscattering images. The backscattering images captured by our imaging flow cytometer system reveal the unique properties of cell nuclei as effective markers for applications such as disease diagnosis, cell classification, and cell cycle monitoring (62). Cellular components with higher concentration of macromolecules exhibit a higher refractive index than the background. These refractive index variations will scatter light when the cell is illuminated by visible light (63, 64). The size and refractive index distributions of the scattering regions determine the angular distributions of the scattered light (65, 66). The majority of human cancers originate in the epithelial cells, so the backscattering imagery can potentially benefit the diagnosis of early cancer and intra-epithelial neoplastic changes. To demonstrate the feasibility of the backscattering imaging

function for cell nucleus monitoring, A549 cells that are going through different life cycles are tested using the imaging flow cytometer.

To observe cells in different stages, A549 cells are cultured with inhibitors to stop their growth at different development stages (67). Mitomycin is used to stop the cell growth at G1 phase where the biosynthetic activities of cells are activated to form necessary proteins for the next phase (S phase). Separately, nocodazole is used to arrest the A549 cells at G2/M phase, more specifically at the prometaphase. Being arrested at the prometaphase, the nuclear membrane breaks down and the constituents of nucleus are distributed within the cytoplasm. Lacking a well-defined nucleus confined by the nucleus membrane, the cell has generally stronger but no well-defined contour in light scattering.

Figure 2.6a shows representative confocal images of stationary cells arrested at G1 phase and prometaphase. Figure 2.6b shows the fluorescence images, backscattering images, and superposition of these two images of travelling cells (0.2m/s) in our imaging flow cytometer. Images acquired by both systems show the general characteristics that cells arrested at G1 phase possess a clearly defined scattering center from the nucleus. In contrast, cells at prometaphase show overall stronger scattering intensities because of higher concentration of nucleic acids and proteins but no well-defined scattering center due to lack of nuclear membrane.

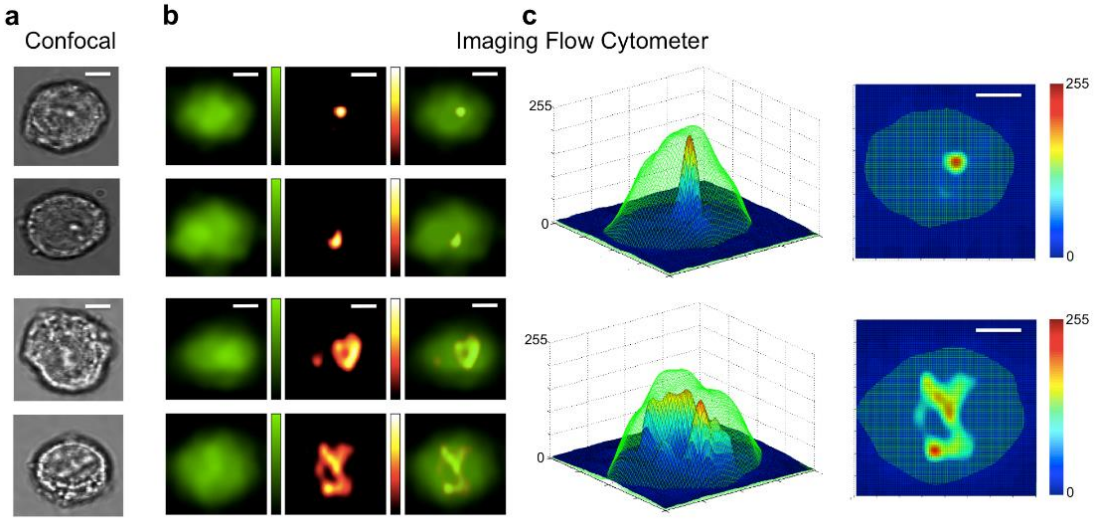

Figure 2.6 Backscattering and fluorescent cell images from spatial-filter-based imaging flow cytometry. All images are of A549 human lung adenocarcinoma epithelial cells, stained with CellTrace CFSE, flowing at a velocity of 0.2 m/s. (a) Representative confocal images of G1 (top two) and G2/M (bottom two) arrested cells. (b) Representative imaging flow cytometer images of G1 (top two rows) and G2/M (bottom two rows) arrested cells. Fluorescence images are shown in left column, backscattering images are shown in middle column, and overlay images are shown in right column. Green colorbar representing intensity from 0 to 255 is applied for fluorescence images. Hot colorbar representing intensity from 0 to 255 is applied for backscattering images. (c) 3-dimensional plots for overlay of fluorescence (green mesh) and backscattering (jet surface) images of G1 (top) and G2/M (bottom) arrested cells. Jet colorbar representing intensity from 0 to 255 is shown. Size of all image crops is 20 μm by 20 μm; all scale bars are 5 μm.

To embody the volume of the scattering cellular components within the cells that are arrested at specific phases, 3-dimensional contour plots for backscattering images overlaid on the fluorescence images are shown in Figure 2.6c. Again, both the backscattering images from the method of spatial-temporal transformation and the confocal images show consistent subcellular features: cells at G1 phase have a condensed scattering center; and cells at prometaphase have a more distributed scattering region.

For traditional flow cytometry, a histogram is one common way to provide information about a cell population or subpopulation. The parameter associated with the histogram is nothing more than fluorescence or scattering intensity. It is more informative if image of every single cell under test is available for flow cytometry tests, so that making decisions about gating can be no longer blind to the sample attributes. Moreover, not only the light intensity can be quantified, but also many morphological measurements can be performed on account of the available images of the cells under tests. Figure 2.7a and Figure 2.7b are scatter plots, which are common result plots in traditional flow cytometer, along with four examples labeled in the plot for the size of backscattering images of cells at G1 phase and G2/M phase, respectively. To compare the backscattering images of cells arrested at G1 and G2/M phase, Figure 2.7c shows the histogram of the Feret's diameter, also known as maximum calliper. The G1 cells, shown in blue bars, tend to have Feret's diameter of 3 to 4 μm, and G2/M cells, shown in red bars, have larger Feret's diameter. Instead of pure numerical expression, Figure 2.7b shows two example backscattering images for each bin from 2 μm to 15 μm in the histogram.

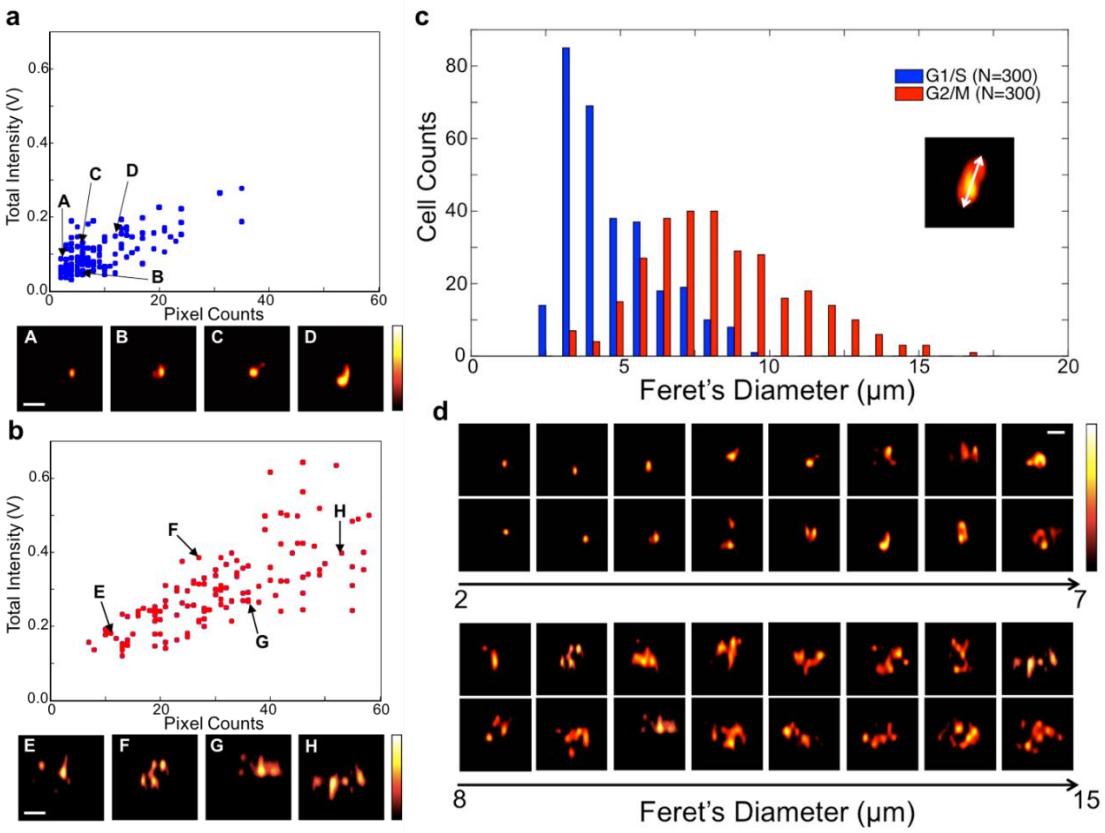

Figure 2.7 Differences of the backscattering images of cell arrested at G1 phase and G2/M phase. All images are of A549 cells flowing at a velocity of 0.2 m/s. (a) Scatter plot for the size (area) of backscattering images of cells at G1 phase, with four image examples labeled in the plot. (b) Scatter plot for the size (area) of backscattering images of cells at G2 phase, with four image examples labeled in the plot. (c) Histogram of the Feret's diameters of the G1 (blue bar) and G2/M (red bar) arrested cells' backscattering images. 300 cell images from each group are measured. The sketch shows the definition of the Feret's diameter: the longest distance between any two points along the object's boundary, also known as maximum caliper. (d) Two example backscattering images for each bin in the histogram. Hot colorbar represents intensity from 0 to 255. Sizes of all cell backscattering images are 20 μm by 20 μm; the scale bar is 5 μm.

2.4 Discussion

We have demonstrated a spatial-temporal transformation technique that enables traditional flow cytometers to capture fluorescence and backscattering images of cells

travelling at high speed in fluid stream. The image quality is comparable to the conventional fluorescence microscopy imaging for still cells using a CCD or CMOS camera. The spatially distributed backscattering plots generated by our system reveal not only the commonality of cells of the same type but also the inhomogeneity of them, exemplified by the same cell type undergoing different life cycles. Because of the simplicity of the design and the use of PMTs rather than CCDs for construction of cell image, our approach can convert or retrofit existing flow cytometers into systems with single cell imaging capabilities. While in our proof-of-concept demonstration, we show imaging results for two parameters (i.e. one-color fluorescence and backscattering), our method can be applied to produce cell images of multiple fluorescent colors with additional dichroic mirrors and PMTs. Furthermore, our method can work at higher fluid flow rate for higher spatial resolution and throughput with high-speed digital data acquisition electronics.

Chapter 2, in part, is a reprint of the material as it appears in *Scientific Reports* 2015, Y. Han and Y.-H. Lo. "Imaging cells in flow cytometry using Spatial Temporal Transformation". The dissertation author was the first author of this paper.

Chapter 2, in part, is a reprint of the material as it appears in *Proceedings of SPIE* 2016, Y. Han and Y.-H. Lo. "Imaging flow cytometer using computation and spatially coded filter". The dissertation author was the first author of this paper.

Chapter 3

Cameraless High-throughput 3D Imaging Flow Cytometer

Increasing demand for understanding the vast heterogeneity of cellular phenotypes has driven the development of imaging flow cytometry (IFC), that combines features of flow cytometry with fluorescence and bright field microscopy. IFC combines the throughput and statistical advantage of flow cytometry with the ability to discretely measure events based on a real or computational image, as well as conventional flow cytometry metrics. A limitation of existing IFC systems is that, regardless of detection methodology, only two-dimensional (2D) cell images are obtained. Without tomographic three-dimensional (3D) resolution the projection problem remains; collapsing 3D information onto a 2D image, limiting the reliability of spot counting or co-localization crucial to cell phenotyping. Here we present a solution to the projection problem: three-dimensional imaging flow cytometry (3D-IFC), a high-throughput 3D cell imager based on optical sectioning microscopy. We combine orthogonal light-sheet scanning illumination with our previous spatiotemporal transformation detection to produce 3D cell

image reconstruction from a cameraless single-pixel photodetector readout. We further demonstrate this capability by co-capturing 3D fluorescence and label-free side-scattering images of single cells in flow at a velocity of 0.2 m s-1, corresponding to a throughput of approximately 500 cells per second with 60,000 voxels (resized subsequently to 106 voxels) for each cell image at a resolution of less than 1 micron in X, Y, and Z dimensions. Improved high-throughput imaging tools are needed to phenotype-genotype recognized heterogeneity in the fields of immunology, oncology, cell- and gene- therapy, and drug discovery.

3.1 Introduction

A central challenge of biology is to correlate the phenotype of heterogeneous individuals in a population to their genotype in order to understand the extent to which they conform to the observed population behaviour or stand out as exceptions that drive disease or the ability to overcome threats to health (68–71). While optical microscopy is a cornerstone method to study the morphology and molecular composition of biological specimens, flow cytometry is a gold standard for quantitative high-throughput single-cell characterization in numerous biomedical applications (72, 73). Recognizing the need to merge these two powerful platforms, several groups have proposed techniques for imaging flow cytometry (IFC) (74). IFC simultaneously produces ensemble-averaged measurements and high-content spatial metrics from individual cells in a large population of cells, without perturbation due to experiment condition change. A important limitation of existing IFC systems is that, regardless of the optical detection method and computation algorithm is used, only 2D cell images can be obtained (45, 75, 76). The absence of 3D

tomography results in occlusion of objects, blurring by focal depth, loss of z-axis spatial resolution, and artefacts due to projection of a 3D cell into a 2D image. For example, with 2D microscopic imaging, if a fluorescent probe is observed at the center of a cell, its location (e.g. membrane, cytosol, nucleus) is ambiguous. For a range of applications, such as internalization measurements, probe co-localization, and spot counting, relative to 2D imaging that is dependent on the cellular orientation to the imaging plane, 3D images provide more complete and accurate phenotyping of cell and organelle morphology, as well as nucleic acid and protein localization to support biological insights. (77). Unfortunately, rapid and continuous 3D image acquisition for single cells in flow has not been available.

Here we present high-throughput three-dimensional imaging flow cytometry (3D-IFC) based on optical sectioning microscopy(78). This combination of light-sheet scanning illumination technique and spatial-temporal transformation detection technique enables fluorescent and label-free 3D cell image reconstruction from single-pixel photodetector readout without a camera (60, 79). Building upon the speed and sensitivity benefits of photomultiplier tube (PMT), the 3D-IFC uses multiple scanning techniques to add spatial information in a fairly conventional flow cytometry architecture amenable to wide adoption. 3D imaging is achieved by laser scanning across the first axis, the cell translating by flow across the second axis, and the use multiple pinholes arranged along the third axis to produce fluorescent and label-free information from 60,000 voxels per cell. By precisely mapping time to space, photodetector readout at one timepoint corresponds to one voxel in a 3D space. Here we demonstrate 3D-IFC of 0-degree fluorescence and 90-degree label-free side-scattering imaging of single cells in flow at a velocity of 0.2 m s^{-1}, corresponding to a throughput of approximately 500 cells per second.

3.2 Methods

3.2.1 Experimental Setup of the 3D-IFC

A schematic of the 3D-IFC system is shown in Figure 3.1. In the 3D-IFC system, suspended cells are 2D hydrodynamically focused single file into a quartz flow cell with a square cross section (80). Laser excitation is via a light-sheet (x-y plane) with a diffraction limited beam waist and a height of 200 to 400 μm, scanning in z-direction at a very high rate (200 kHz). When a cell flowing through the whole optical interrogation at 0.2 m s^{-1}, a pixelated field of view is represented by a 3D space with X by Y by Z voxels as shown in Figure 1c. A pinhole array on the spatial filter is aligned at a tilting angle, ϑ, to the flow stream, so the pinhole array also steps along x-direction. In this manner, each pinhole allows light from voxels with a distinct x-index to pass to PMT detector (see Methods for mask details). The imaging process begins when a flowing cell appears at the first pinhole of the spatial filter. During the first light-sheet scanning period (5 μs), light intensity of voxels $z_{1-\mathrm{Z}}$ with x_1y_1 index is collected. As the cell flows downstream in y to the next position, x_1y_2, the corresponding $z_{1-\mathrm{Z}}$ voxels are produced. This is repeated until cell completely passes pinhole 1 when the whole 2D yz-slice at x_1 is imaged. As the cell travels farther downstream in y, it reaches the following pinholes and yz-slices of at x_2 to x_X are recorded.

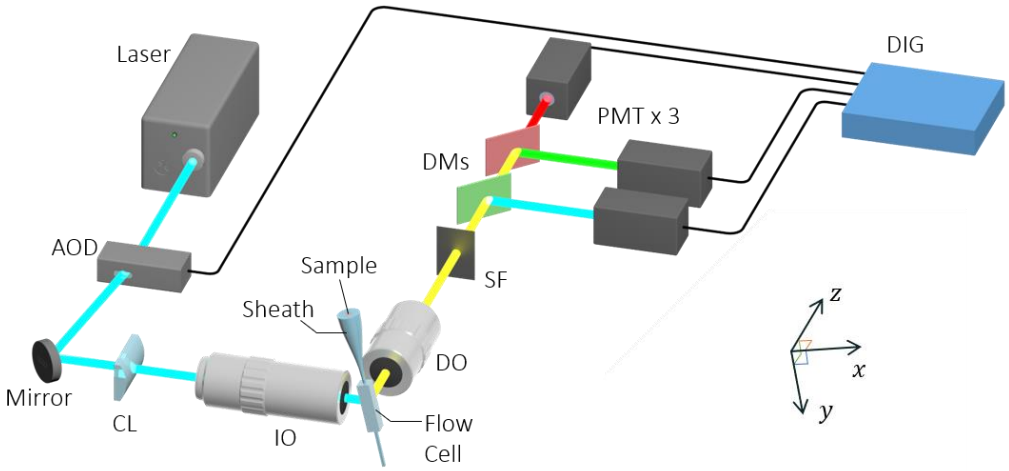

Figure 3.1 Schematic diagram of the 3D-IFC system. AOD, acousto-optic deflector; CL, cylindrical lens; IO, 50X/0.55 illumination objective lens; DO, 10X/0.28 detection objective lens; SF, spatial filter; DMs, dichroic mirrors; PMT, photomultiplier tube; DIG, 125 MS s^{-1} digitizer. The AOD and CL produce a scanning light-sheet. Sample is 2D hydrodynamically focused by sheath before entering the square cross section quartz flow cell.

To precisely measure the speed of each cell for image reconstruction by the spatiotemporal transformation, pairs of slits upstream and downstream of the pinholes are added to the optical spatial filter (Figure 3.3). The measured rate of the cell moving through the detection zone, and the known frequency of the light-sheet scanning rate ensures each voxel in a 3D-IFC image has a distinct time-domain value, and all voxels can be discreetly captured in time from single-element PMT. 3D cell images are then reconstructed from the time-domain signal. A detailed description and mathematical formulation are included in the following section.

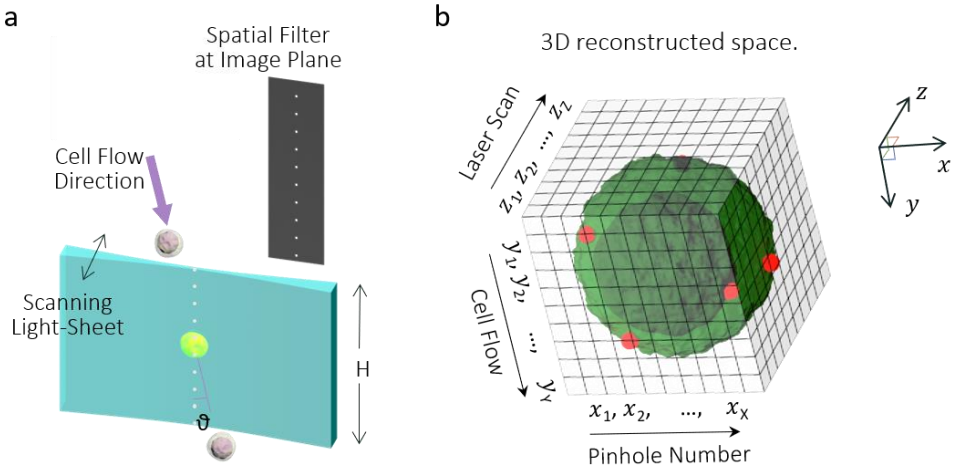

Figure 3.2 **(a)** Optical interrogation area. H, height of the light-sheet; ϑ, tilt angle between flow (y-axis) and vertical line. Illumination light-sheet propagates horizontally and scans in z-axis, sample flows in y-axis, x is the orthogonal axis. The spatial filter at the image plane uses pinholes to produce line scans across the x-axis. **(b)** 3D reconstructed space. The resolution on the x-axis is determined by the number of pinholes (pixelated field of view in x-direction); resolution of y by the distance between two slits (pixelated field of view in y-direction); and resolution of z by the light-sheet scanning range (pixelated field of view in z-direction).

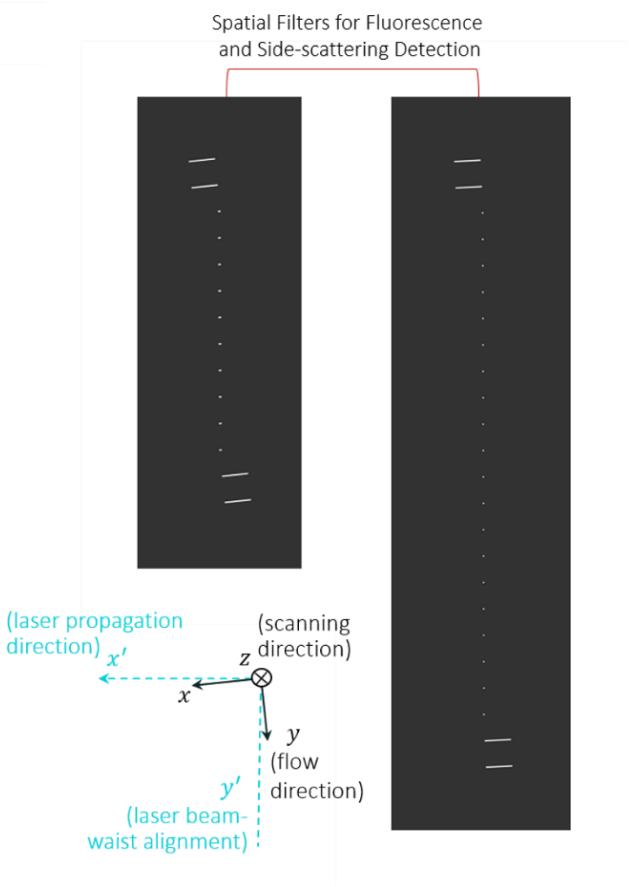

Figure 3.3 Two examples of spatial filters placed at image plane. The top two and bottom two long slits with dimensions of 10 µm by 200 µm are for speed detection. The other pinholes on the spatial filter are 10 µm by 20 µm (left) and 10 µm by 10 µm (right), for 3D image capturing with pixel size of 2 µm and 1 µm in x-direction, respectively. The arrangement of the pinhole array aligns with the laser beam-waist.

3.2.2 3D Image Detection and Construction Algorithm

The optical system is arranged in a light sheet fluorescence microscopy configuration (Figure 3.1), which only illuminates a specimen in a single plane at a time whilst the signal is detected in a perpendicular (z-) direction (Figure 3.2a). An acousto-optic deflector (AOD) is producing the high-speed, 200 kHz in this implementation, scanning in z-direction. A single-pixel photodetector detects fluorescence or scattering

light passed the spatial filter in each channel, and an image is reconstructed from the time-domain output. The pinholes on the spatial filter is arranged vertically. The flow (y-) direction is tilted to create an angle ϑ (Fig. 1b), which is determined by the field of view in x-direction D_x, the field of view in y-direction D_y and number of pinholes X, $\vartheta = \tan^{-1}(D_x/(X \cdot D_y))$. Also, because the z-direction illumination light-sheet scans over a range that is larger than the cell size, and at a speed that is much higher, typically more than 20 times higher than the cell travelling speed in y-direction, when cell passing one pinhole, the light intensity of one yz-plane image slice is recorded; when cell passing the next pinhole, another yz-plane image stack is acquired. Combining the scanning light-sheet, the cell's flow motion, and the spatial filter, the detector only detects the fluorescence of an individual voxel in the cell at a time, which allows one-to-one time to space mapping. The concept can be mathematically formulated in the following equations. The measured PMT signal $S(t)$ can be expressed as

$$S(t) = \iiint \left\{ \iint C(x', y' - v_c t, z) I(z, t)\, psf(x - x', y - y') dx' dy' \right\} F(Mx, My)\, dxdydz \qquad \text{Eq. 3-1}$$

$$S(t) = \iiint \{C(x, y - v_c t, z) I(z, t)\} \otimes psf(x, y, z)\} \cdot F(Mx, My) dxdydz$$

, where $C(x, y, z)$ is the 3D cell fluorescence or scattering light intensity profile (Figure 3.2b), $I(z, t)$ is the light-sheet illumination, $F(x, y)$ is the characteristic function of the spatial filter, v_c is the cell flowing speed, M is the magnification factor of the detection system.

The acoustic frequency sent to the acoustic transducer in the AOD is varied to deflect the beam to create illumination at different z-position. The tuning voltage that produce continuous change of acoustic frequency can be generated by various types of waveforms, such as sinusoidal, triangle, etc. For the most laser power efficient, the tuning voltage is set to be changing in a sawtooth manner, so the position of the light sheet in z-direction $z_0(t)$ can be described as

$$z_0\big(t \in (nT, (n+1)T)\big) = v_i(t - nT), \qquad n = 0,1,2,\ldots \qquad \text{Eq. 3-2}$$

, where T is the light-sheet illumination scanning period, v_i is the scanning speed in z-direction.

By using the cylindrical lens, the laser is diverged to form a light-sheet with a height in y-direction of 200-400 μm. The scanning light-sheet illumination $I(z,t)$ can be described as Gaussian beam:

$$I(z,t) = k \cdot e^{-\frac{\left(z - z_0(t)\right)^2}{\sigma^2}} \qquad \text{Eq. 3-3}$$

With oversampling PMT signal readouts, the spatial resolution in z-direction is diffraction limited. The Gaussian beam waist is measured 0.73 μm and is approximated as a delta function for simpler calculation:

$$I(z,t) \approx k \cdot \delta\big(z - z_0(t)\big) \qquad \text{Eq. 3-4}$$

Two examples of the spatial filter are shown in Figure 3.3. Putting the slits used for speed detection aside, the characteristic function $F(x,y)$ of the spatial filter is designed to be

$$F(x,y) = \sum_{q=1}^{N} \delta\big(x - x_q\big) \cdot \delta\big(y - y_q\big) \qquad \text{Eq. 3-5}$$

, where $q = 1,2, \dots, N$ is the number of pinholes on the spatial filter. The size of the pinhole, together with the NA of detection objective lens, the cell flowing speed, and signal sampling rate determine the spatial resolution in x- and y-directions. The spatial filters are fabricated using electron beam lithography and the blackout area is made of chromium with a thickness of 250 nm.

With the approximations above, when $y_{q+1} - y_q > cell\ size$, and cell projection is overlapped with j-th pinhole,

$$S(t) = \int_{x,y} C\left(x, y - Mv_2 t, z_0(t)\right)\delta\left(x - x_q\right) \cdot \delta\left(y - y_q\right)dxdy$$
$$= C\left(x_j, y_j - Mv_c t, z_0(t)\right) \quad \text{Eq. 3-6}$$

Presuming cell is within the depth of field, and the system PSF at multiple z is not considered. The light intensity signal detected by PMT (Hamamatsu) is first amplified by an amplifier (Hamamatsu) with a bandwidth from DC to 150 MHz, and then digitized by a digitizer (ADVANTECH) with a maximum sampling rate of 125 MS/s per channel.

Consequently, this approach maps the 3D cell image into the time-domain light intensity on a one-to-one basis. The 3D image construction algorithm is realized in MATLAB according to the equation above. Due to slight variance in flowing speed v_c of cells, the original size of the 3D image of each cell can be slightly different. The original 3D image is then resized to 100 x 100 x 100 pixels. 3D image batch processing is performed in ImageJ.

3.2.3 Microfluidic System

The microfluidic system (Extended Data Figure 1a) continuously introduces suspended cells to the optical interrogation area. Since the position of the cells in the cross-section of the microchannel is aligned with the optical field of view in all the x-, y- and z-directions, a reproducible and stable flow speed for cells is obtained by tightly focusing the cells at the center of the square cross-section. Suspended cells in a sample injected by a syringe pump are hydrodynamically focused into a single stream. A sheath flow is used to confine flowing cells in both x- and z-direction. An air pressure pump together with a liquid flow meter are used to provide stable sheath flow. At the junction of sheath flow and sample flow, tubing ends are specially tapered to keep symmetric flow. The flow rate ratio between the sample and sheath is precisely controlled to be 100:1 to ensure particles flowing at a high speed and within the optical field of view.

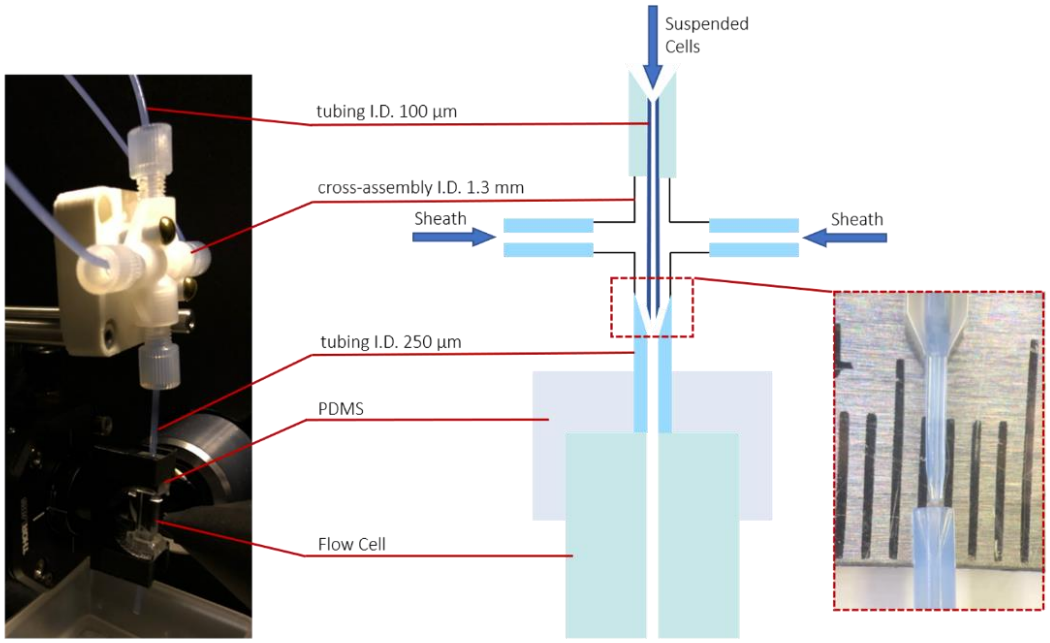

Figure 3.4 Microfluidic system in the 3D-IFC together with picture of specially engineered tapered tubing. The flow through channel in the quartz flow cell has a cross-section dimension of 250 µm by 250 µm and a length of 20 mm.

3.2.4 Mapping Time-domain Signal to 3D Space

Figure 3.5 shows the typical output of the 3D-IFC system. The detected time-domain multi-parametric signals (multi-color fluorescence, FL1 and FL2, and side-scattering, SSC, light intensities) are synchronized with the reference output of the tuning voltage of the AOD driver, which denotes the z-position of the detected voxel. At a 200 kHz scanning rate, a one-dimensional (1D) intensity profile in z-axis is recovered from the time-domain signal within a time period of 5 µs (Fig. 3.5a). During the ~100 µs of cell travel between pinholes, ~20 periods of laser scanning are performed, and an yz-plane 2D image array is recovered from the PMT readout (Fig. 3.5b). As the cell travels through the

entire interrogation area, a stack of 2D yz-plane images are recovered, and the final 3D image is reconstructed, with the ordinal pinhole number indicating the voxel's x-position. In the example shown in Figure 1f, a 10-pinhole spatial filter produces 10 2D yz-plane images and a signal length of 1 ms, corresponding to a throughput of 500 cells per second. The bandwidth of PMT and digitizer, 150 MHz and 125 MHz, respectively, in this implementation, supports the throughput at 60,000 voxels per 3D cell image. Each 3D cell image in a 3D space of 20 μm by 20 μm by 20 μm, is resized to 100 by 100 by 100 pixels for 3D image analysis and quantitative measurements.

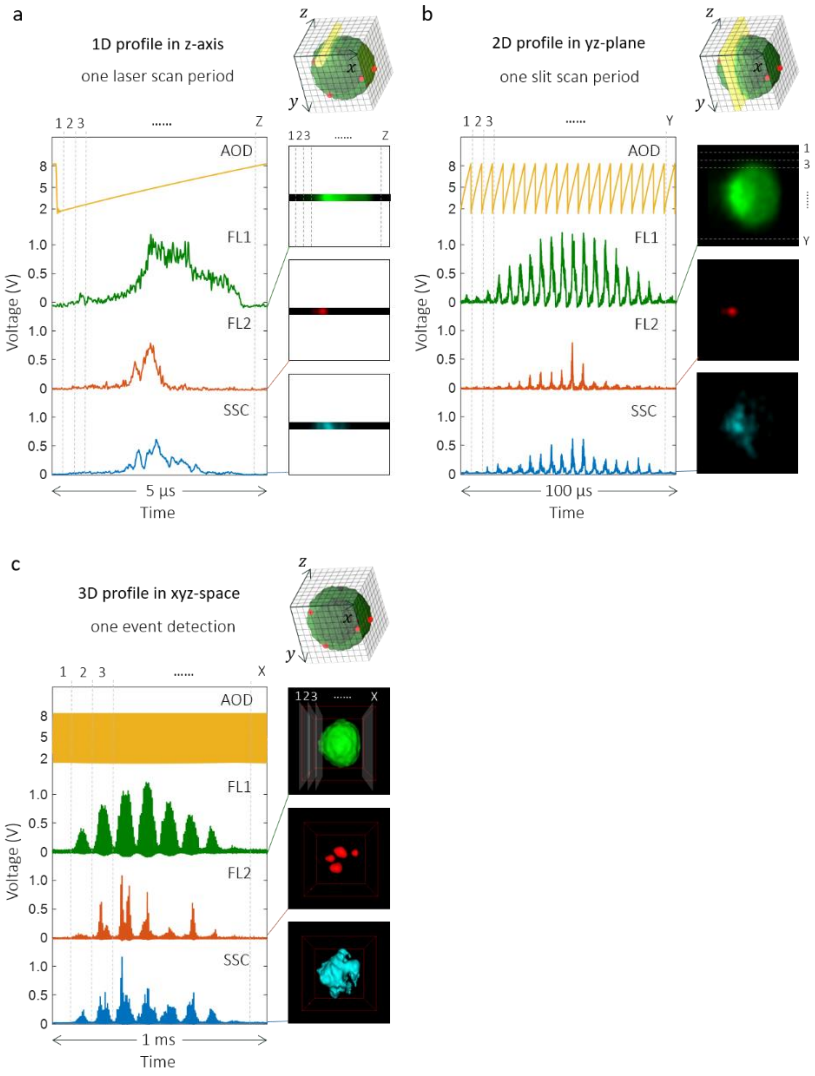

Figure 3.5 Demonstration of Time to 3D-space Mapping. AOD, tuning voltage of the AOD driver; FL1, PMT readout of fluorescence detection channel 1; FL2, PMT readout of fluorescence detection channel 2; SSC, PMT readout of side-scattering light detection channel. **(a)** One light-sheet scan period produces 1D light intensity profile in z-axis. The PMT voltage readout of one timepoint corresponds to the light intensity of one voxel in z-axis. **(b)** While object travels along y-axis, multiple scans produce a 2D profile in yz-plane within one pinhole scan period. Each section—separated by dotted lines—corresponds to the light intensity of one row in the 2D image stack. **(c)** When object completely passes through the spatial filter covering area, the time-domain signal contains the complete information of the 3D profile in xyz-space. Each section corresponds to one 2D image slice. X, number of pinholes (pixelated field of view in x-direction); Y, distance between two slits (pixelated field of view in y-direction); Z, light-sheet scanning range (pixelated field of view in z-direction).

3.2.5 3D Image Processing

Processing of the raw 3D images obtained by the 3D-IFC is performed in ImageJ. First, 3D Gaussian filtering and linear contrast enhancement with stack histogram stretching are performed. Then, the plugin 3D Viewer is applied to produce rendering views (Surface, Volume, and Orthoslice) of 3D images. For merged images, images from two-color fluorescence detection channels are merged. In the intensity histograms, black bars are in linear scale from 0 to 255, and the grey bars are in log scale. Finally, the 3D Object Counter (OC) is used to perform spot counting and object measurements including morphological and intensity-based parameters.

3.2.6 Cell Sample Preparations

(1) Cell with Fluorescent Beads. The human embryonic kidney 293 (HEK-293) cells were cultured with complete culture media (DMEM, 10% Fetal Bovine Serum, 1% Penicillin Streptomycin) to 90% confluency in 10 cm petri dish. After 100X dilution of the 1.0 μm fluorescent beads (Ex/Em: 488/645 nm, T8883, Thermo Fisher) from the stock solution (2% solids), 100 μL of the diluted solution was mixed with 10 mL fresh cell culturing media and added to cell culturing plate. After continuous culturing for 10 hours, the HEK-293 cells were harvested and stained with CellTrace CFSE cell proliferation kit (Ex/Em: 492/517 nm, C34554, Thermo Fisher) at a working concentration of 20 μM. After the staining process, cells were fixed by 4 % paraformaldehyde, washed and resuspended in 1X phosphate buffered saline (PBS). Before every imaging experiment, the cell suspension was diluted in PBS to a concentration of 1000 cells/μL.

(2) CFSE Staining. The HEK-293 cells were first cultured with complete culture media to 98% confluency in 10 cm petri dish, and then were harvested and resuspended to a concentration of $1x10^6$ cells/mL in 1X PBS. The CFSE Cell Proliferation Kit (Ex/Em 492/517nm, C34554, Thermo Fisher) were added to the cell suspension at a working concentration of 20 μM. After incubating the cells at 37℃ for 30 minutes, fresh culture media (DMEM) were used to quench the staining process and the HEK-293 cells were washed by 1X PBS and fixed by 4 % paraformaldehyde. The fixed cells were washed and resuspended in 1X PBS. Protocol is also applied to stain CMK3 cells and human blood leukocytes.

(3) PKH67 Cell Membrane Staining. The HEK-293 cells were first cultured with complete culture media (DMEM, 10% Fetal Bovine Serum, 1% Penicillin Streptomycin) to 98% confluency in 10 cm petri dish, and then harvested and resuspended to a concentration of 10^6 cells/mL in 1X PBS. After washing with 1X PBS, cells are resuspended to a concentration of $2x10^7$ cells/mL in Diluent C buffer from the PKH67 Fluorescent Cell Linker Kit (Ex/Em 490/502nm, PKH67GL, Sigma-Aldrich). The suspended cells were mixed with PKH67 ethanolic dye solution at a working concentration of 50 μM. After 5 minutes incubation, the staining was quenched by 1% BSA solution and the stained cells were washed by 1X PBS and fixed by 4 % paraformaldehyde. The fixed HEK-293 cells were washed and resuspended in 1X PBS.

(4) CMK3 Cell Irradiation Treatment and Immunostaining. The human glioblastoma CMK3 cells were cultured with complete culture media (DMEM-F12, 2% B27 supplement, 1% Penicillin Streptomycin, 1% Glutamax, 100 μg/L EGF, 100 μg/L FGF, 0.24% Heparin) in culture plates. The cells were harvested and resuspended to a

concentration of $1x10^6$ cells/mL in 1X PBS, and then stained with CFSE. To induce DNA double-strand breaks (DSB), CMK3 cells are treated with 6 Gy irradiation by Cesium source irradiator. The treated cells were washed once with 1X PBS and fixed with 1% paraformaldehyde 30 minutes post irradiation. The fixed cells were washed with PBS twice. Then 70% ethanol was added to the cells and the cells were incubated on ice for 1 hour. After ethanol treatment, cells were washed with PBS twice and incubated in 1% TritonX-100 at room temperature for 10 minutes. Then, cells were washed with PBS once and incubated in 5% Bovine Serum Albumin (BSA) in PBS for 30 minutes at room temperature on shaker. Cells were then washed with PBS once and incubated in Anti-phospho-Histone H2A.X (Ser139) Antibody, clone JBW301 at 1:300 dilution on ice on shaker for 1 hour. After the primary antibody treatment, cells were washed twice with 5% BSA and incubated in PerCP/Cy5.5 anti-mouse IgG1 Antibody at 1:100 dilution on ice on shaker for 1 hour. At last, the stained cells were washed twice with 5% BSA and resuspended in 1:3 diluted stabilizing fixative buffer in MilliQ water. Before every imaging experiment, the cells ware diluted in PBS to a concentration of 500 cells/μL.

(5) Leukocytes Separation and staining. The fresh human whole blood was harvested in EDTA tube from San Diego Blood Bank. The red blood cells in the whole blood were first lysed by RBC lysis buffer (00-4300-54, Invitrogen) and the leukocytes population was harvested by soft centrifuge after the lysing process. The harvested leukocytes were then washed and resuspended to a concentration of $1x10^6$ cells/mL in 1X PBS. The resuspended leukocytes were stained with CFSE. After the staining process, the cells were fixed by 4 % paraformaldehyde, washed and resuspended in 1X PBS. Before

every imaging experiment, the cell suspension was diluted in PBS to a concentration of 500 cells/μL.

3.3 Results

To demonstrate the imaging capability of 3D-IFC system on various biological samples, we imaged suspended single cells flowing at a speed of 0.2 m s^{-1}. The following sections present two-color fluorescence and dark-field (side-scattering) 3D images of various mammalian cells.

3.3.1 Fluorescence Cells and Beads Imaged by the 3D-IFC

In Figure 3.6, HEK-293 cells were stained with an intracellular carboxyfluorescein dye (CFSE) and bound with a random number of 1 μm fluorescent carboxylate-modified polystyrene beads. Figure 3.6 shows that while 2D bead images overlapped, the 3D-IFC resolved the exact number of particles from the reconstructed 3D images, which is crucial for localizing and co-localizing (81, 82). In a flow system, cells and their internal structures are orientated at random, as a result 2D images may be from an unfavorable viewing perspective. Multiple perspectives can be achieved via 3D-IFC cell tomography to provide improved relative position relationships and spot counting results, which favors both machine vision and human visualization.

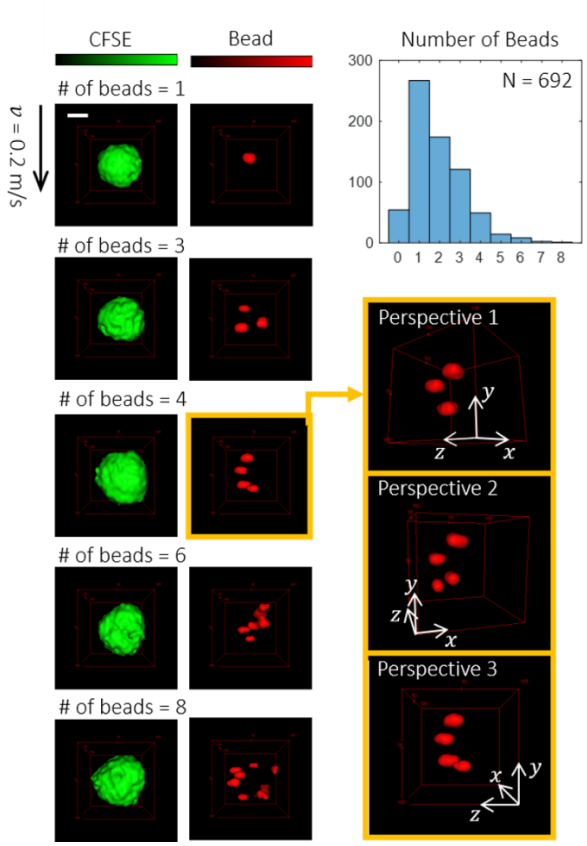

Figure 3.6 Cells and beads imaged by the 3D-IFC. Representative 3D images of CFSE-stained HEK-293 cells bound with different number of 1 μm fluorescent beads and histogram of 692 detection events. The explicit relative position relationship in 3D space indicates that the particle counting in the 3D-IFC is independent of cell orientation. In the example of cell bound with 4 beads, occlusion in specific perspective is an inevitable source of error for particle counting with 2D images. Scale bars, 5 μm. Flow speed 0.2 m/s. CFSE, intracellular carboxyfluorescein dye, Ex/Em: 488/517; Bead, carboxylate-modified microspheres, Ex/Em: 488/645.

3.3.2 Membrane-Fluorescent Cells Imaged by the 3D-IFC

Protein localization and trafficking is another application of high-throughput 3D imaging measurement20. HEK-293 cells are stained by a general membrane dye (PKH67) are shown in Figure 3.9. The cross-sectional views extracted from 3D cell images show hollow patterns, representing presence of fluorophores on the membrane.

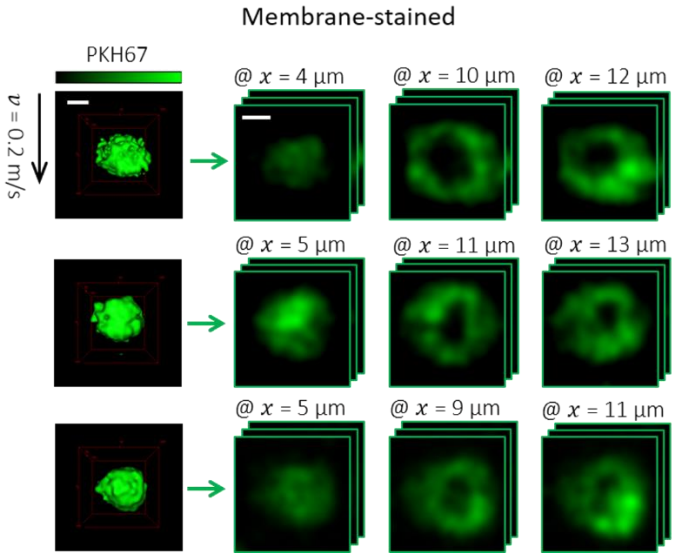

Figure 3.7 Membrane Fluorescent Cells Imaged by the 3D-IFC. Representative 3D images of HEK-293 cells with fluorescent cell membrane. The flow speed of all the cells are 0.2 m/s. PKH67, general cell membrane dye, Ex/Em: 490/502. Scale bars, 5 µm.

3.3.3 Fluorescent γH2AX Foci in DNA-damaged Cells

When ionizing radiation or cytotoxic chemical agents cause DNA damage in the form of double stranded breaks (DSBs), the phosphorylated protein gamma-H2AX (γH2AX) quickly forms foci at DSBs in a 1:1 manner (83). With anti-γH2AX immunolabeling, foci reflect DNA damage and ability for DNA repair (84). 2D imaging techniques and manual quantification are used today, but counting foci from 2D images is labor intensive and unreliable due to perspective dependence (85). To evaluate foci counting of the 3D-IFC system, we imaged immunolabeled γH2AX foci in CMK3 cells (a glioblastoma multiforme cell line) after 6 Gy of gamma-irradiation. Representative cell images are shown in Figure 3.10.

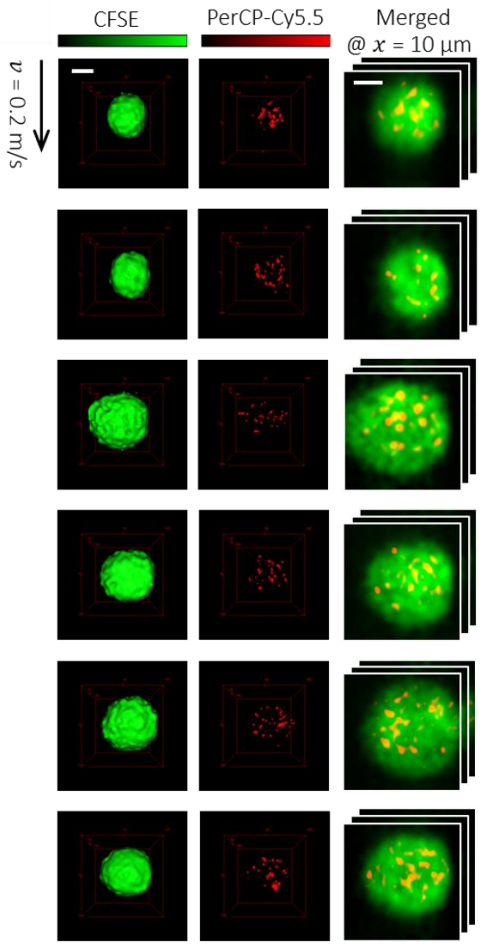

Figure 3.8 Fluorescent γH2AX foci Imaged by the 3D-IFC. Representative 3D images of irradiation damaged glioblastoma CMK3 cells stained with CFSE and γH2AX antibody conjugated PerCP/Cy5.5; and their two-color fluorescence 2D yz-plane merged image slices at x = 10 µm. The high quality of the 3D images shows that the 3D-IFC is suitable for DNA-damage foci related study. Scale bars, 5 µm. The flow speed 0.2 m/s. Ex/Em: 488/517; PerCP-Cy5.5: DNA-damage antibody conjugated dye, Ex/Em: 490/677.

The data show that the number of γH2AX foci is unrelated to the fluorescence intensity, thus intensity-based measurements with conventional flow cytometry metrics poorly reflects DNA damage (Figure 3.11). In contrast, the 3D-IFC system enabled accurate and rapid analysis of the number of γH2AX-positive foci.

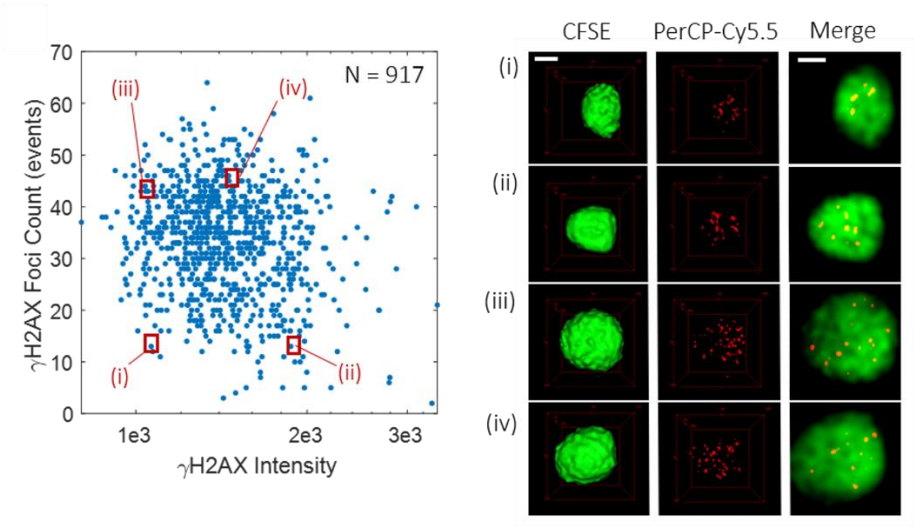

Figure 3.9 Scatterplot of 917 detection events in the γH2AX intensity and foci count together with images of the cells within the marked regions (i)–(iv) in the scatterplot. The data show that foci count is unrelated to the fluorescence intensity from labelled γH2AX, thus intensity-based measurements with legacy flow cytometers are unable to evaluate the extent of DNA damage. Scale bars, 5 μm.

3.3.4 Side-scattering Image Captured by the 3D-IFC

Using the side-scatter dark-field imaging mode, the 3D-IFC is able to generate a 3D spatial distribution of scattered light. It is known that refractive index variations will scatter light when the object is illuminated by visible light, and the size and refractive index distributions of the scattering regions determine the distributions of the scattered light. The 3D SSC images represent the spatial distribution of those refractive index (n) variations among the fluid (PBS, n~1.335), the cells (n~1.3-1.6) and the polystyrene beads (n~1.6) (86, 87). Figure 3.10 shows two-color fluorescence and unlabelled dark-field (90-degree side-scattering) 3D images of CFSE-stained HEK-293 cells with 1 μm fluorescent beads bound to cell.

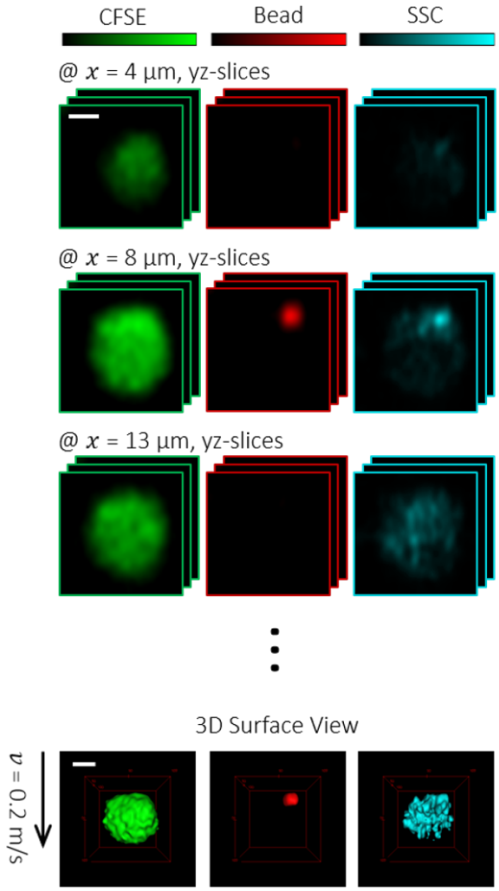

Figure 3.10 CFSE-stained HEK-293 cells with 1 µm fluorescent beads bound to cell. Recovered 2D yz-plane images and the assembled 3D surface-rendered view (bottom row) of CFSE fluorescence, bead, and SSC. The flow speed of all the cells are 0.2 m/s. CFSE, intracellular carboxyfluorescein dye, Ex/Em: 488/517; Bead, carboxylate-modified fluorescent microspheres, Ex/Em: 488/645; SSC, 90-degree side-scattering. Scale bar in 2D image stack is 5 µm. The red wireframe in all the 3D views represents a 20 µm by 20 µm by 20 µm 3D space. The same in other Figures.

High sensitivity and large dynamic range of the SSC signal allows analysis at different intensity level, so that strong SSC signal produced by beads and weaker SSC signal produced by cell components can be simultaneously detected. As shown in Figure 3.12, intensity-based low-pass filtered SSC image indicates cell volume, and high-pass filtered SSC image correlates with the fluorescent image of beads.

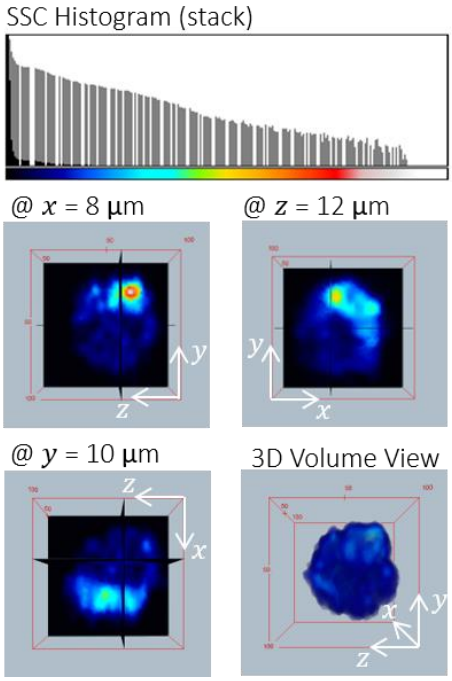

Figure 3.11 Intensity histogram of SSC signal of the cell shown in 3.10 and its 3D profile in Orthoslice view and Volume view.

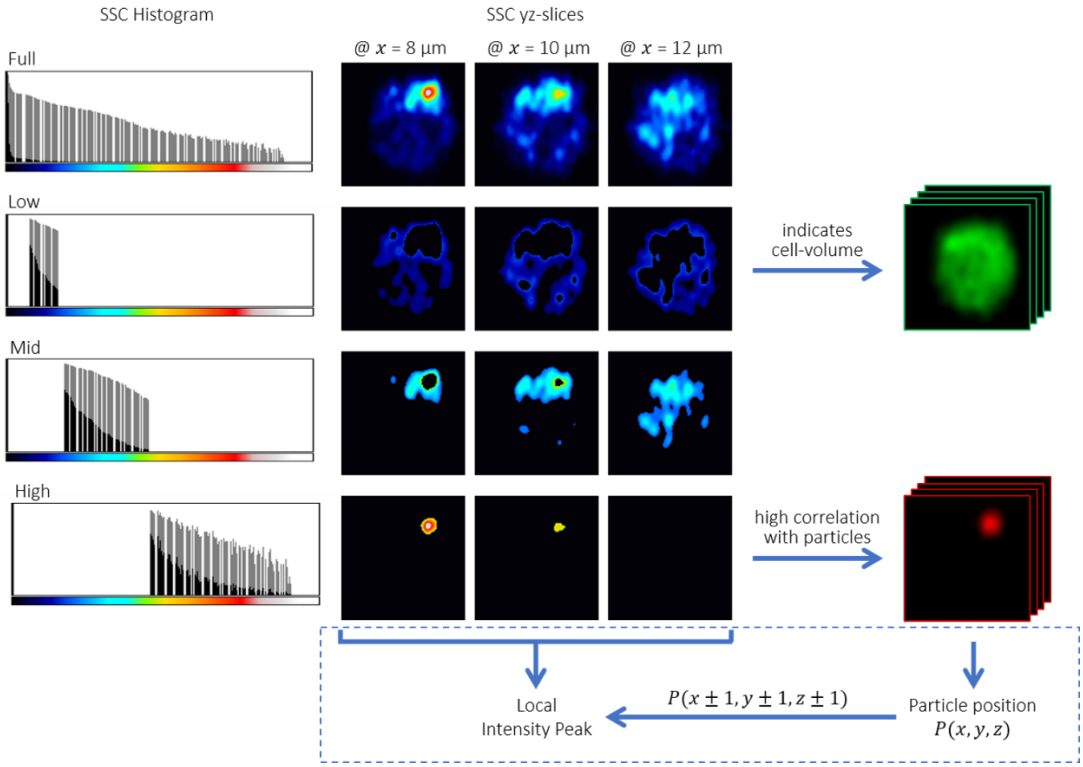

Figure 3.12 Intensity-based Processing of 3D SSC Images. Intensity histograms of 3D SSC image of the cell shown in Figure 3(a). Intensity-based low-pass filtered SSC image indicates cell volume; high-pass filtered SSC image correlates with the fluorescent image of beads. $P(x, y, z)$ is the position of 1 µm size bead determined using 3D fluorescent image; within each bead position's ± 1 µm area, the local intensity peak in 3D SSC image can be found. Scale bars, 5 µm.

3.3.5 Human Blood Leukocytes Imaged in 3 Imaging Modes

With additional optical component and a spatial filter, the 3D-IFC is also extended to simultaneously obtain 2D transmission image of cells. Figure 3.12 shows the schematic diagram of the 3D-IFC system in the configuration with three imaging modes.

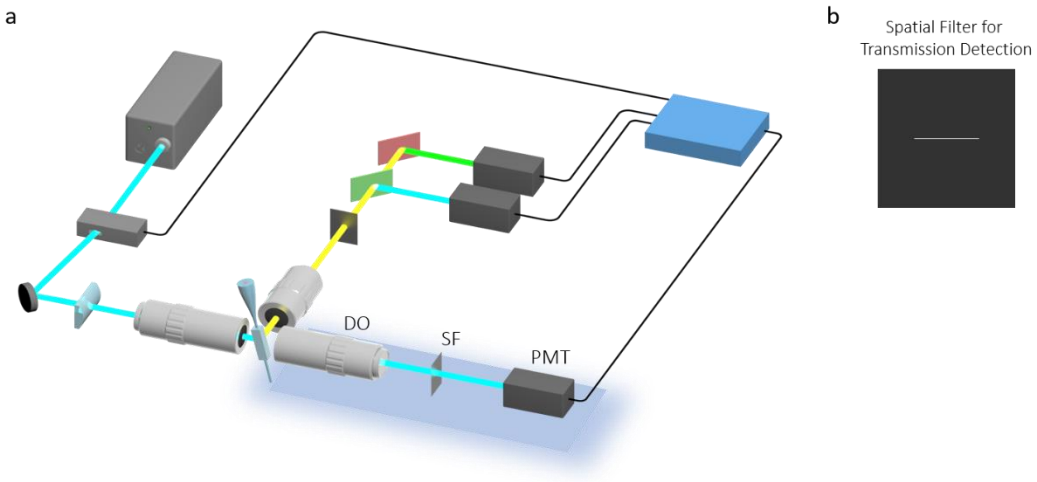

Figure 3.13 Implementation of 2D Transmission Imaging Mode. **(a)** Schematic diagram of the 3D-IFC with transmission imaging mode. Shadowed part is added for transmission image detection. DO, 50X/0.55 detection objective lens; SF, spatial filter; PMT, photomultiplier tube. **(b)** Spatial filter for transmission detection. Single slit with dimensions of 50 µm by 2 mm.

Peripheral blood leukocyte morphology is important clinical diagnostic and prognostic measure for acute and longitudinal evaluations. Figure 3.13 shows representative 3D-IFC imagery of leukocytes in three imaging modes: 2D transmission image and 3D fluorescence and side-scattering images.

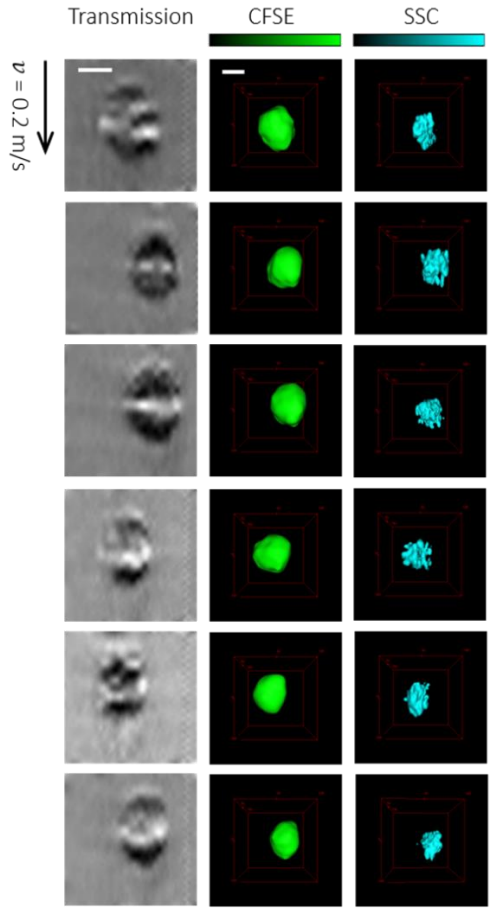

Figure 3.14 Leukocytes Imaged by the 3D-IFC. The flow speed of all the cells are 0.2 m/s. Representative 2D transmission images (left column) and 3D images of leukocytes. Scale bars, 5 µm.

The leukocyte SSC signal not only indicates nuclear granularity but also gives provides cell volumetry obtained from low intensity (low refractive index) SSC imaging. Here two or more intensity bands of 3D SSC signal can be used to generate two or more images that reflect their corresponding refractive indices, such as the cytosol and nucleus, whereas conventional flow SSC intensity signal is dominated by contributions of the nucleus. As shown in Figure 3.14, we can use 3D SSC image to produce cell volume that matches the transmission and fluorescence results.

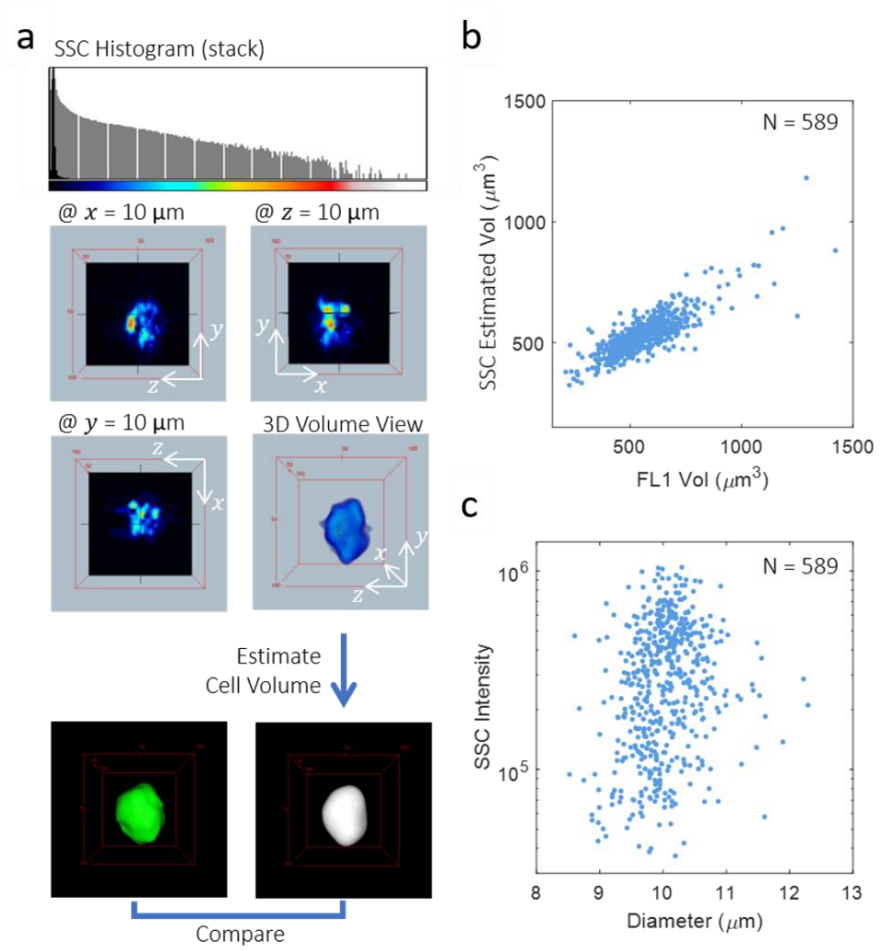

Figure 3.15 **(a)** Intensity histogram of SSC signal of a representative cell and its 3D profile in Orthoslice view and Volume view. Cell volume estimation based on 3D SSC image matches the fluorescence volume. **(b)** Scatterplot of 589 detection events in the CFSE (FL1) volume and SSC-based estimated cell volume. **(c)** Scatterplot in the cell diameter calculated from SSC-based estimated cell volume and SSC intensity.

3.4 Discussion

Through a confluence of several technological discoveries, we have demonstrated that 3D-IFC provides an unprecedented access to high-throughput 3D image capture and analysis. This implementation of 3D-IFC features a cell flow speed of 0.2 m s^{-1}, a spatial resolution of 1 µm in 3 axes, a field of view of 20 µm in all axes, and a throughput of 500

cells per second. The design has the flexibility to directly increase the spatial resolution, field of view and 3D image capture rate through the change of spatial filter and the use of higher flow rate. Its information-rich 3D dark-field (side-scattering) image detection, coupled with 2D transmission image, offers possibilities for label-free assays. Potential applications, such as asymmetric division of T-cells into effector and memory cells (88), the secretory pathway of B cells, phenotype drug discovery (89, 90), protein or receptor translocations (91, 92), tracking of organelle formation or trafficking (93), and chromosome structural aberrations (94), where 3D orientation and polarity are important, could greatly benefit from this 3D-IFC technology, especially in future integrations with image-based sorting functionality (95, 96).

Chapter 3, in part, has been submitted for publication of the material, Y. Han, R. Tang, Y. Gu, A. C. Zhang, W. Cai, V. Castor, S. H. Cho, W. Alaynick, and Y.-H. Lo. "Cameraless high-throughput 3D imaging flow cytometry". The dissertation author was the first author of this paper.

Chapter 4

Summary and Outlook

4.1 Summary of Dissertation

Throughout this dissertation, we have invented the spatial-temporal transformation technology, developed a high-throughput cameraless 3D imaging flow cytometry, and explored the applications of this advanced platforms for imaging and analysis of single cells. From the aspect of system functionality, we expatiated the operating principle and experimental implementation. From the aspect of its power and broad utility, we covered experiments on a variety of cell samples carried out by the 3D-IFC system and presented high-quality cell imagery. This technology is highly versatile and expected to be an enabler to connect phenotype and genotype studies in the fields of immunology, oncology, cell- and gene- therapy, and drug discovery, where heterogeneity is recognized.

4.2 Outlook: High-throughput and Real-time Image Analysis

One of the biggest challenges of 3D-IFC lies in acquiring, storing and processing massive amount of cell images (56, 97, 98). There are many software packages and tools for use in high-throughput image analysis, mainly for microscopy platforms, including

CellProfiler and ImageJ, but in general, the pipelines of these tools are for offline image analysis (55). Fortunately, some of the difficult image processing problems in high-throughput microscopy and LSC can be avoided in IFC. For example, due to cell-to-cell and cell-to-substrate adhesion, strategies for image segmentation such as threshold, watershed and edge-detection have been under development for decades, yet still a bottleneck of the automated image analysis in microscopy. This problem is of little effect in IFC where the cells are put in suspension and interrogated on a single-cell basis (99–103). For blood cells, bone marrow cells, and many cancer cells flowing in the blood vessels, IFC is the most promising approach to study their morphological changes.

Compared to data format in conventional flow cytometry, including integral, peak and width of light intensity, cell images produced by IFC, especially 3D-IFC, are much more complex. Since the 3D-IFC can produce hundreds to thousands of multi-spectral 3D cell images per second, files generated the 3D-IFC can tremendously burden the digital image transportation and processing realized by the back-end data handling unit. Assuming a field of view of 40 μm by 40 μm by 40 μm is represented by a 3D image of 100-pixel by 100-pixel by 100-pixel, at least 1 GB data are generated in one second at a throughput of 500 cells per second. Therefore, a test of a few minutes can easily create a data file beyond 1 TB. For a possible solution, compressive sensing theory-based method has recently been explored to build analog compression directly into the acquisition process so that the sampling can be significantly more efficient (104, 105). Some machine learning techniques can also be applied to data processing for richer information carried out by the 3D-IFC systems (102, 106).

Computational requirements for high-throughput 3D IFC platforms are unprecedented. In order to combine cell sorting with the 3D-IFC to fully realize its tremendous potential, real-time 3D image construction and analysis is required. Hence the ability to produce, measure, analyze 3D cell images, and to sort cells in a real-time manner will be the next major milestone for 3D IFC systems. Possible approaches to extract cell characteristics in real-time include use of field-programmable gate arrays (FPGA) or Graphics Processing Unit (GPU) to implement various image processing and machine learning algorithms.

With the advent of big-data era, life scientists started to grapple with massive volumes of data. Recent advances in high-throughput IFC and 3D-IFC allows continuous high-throughput capture of cell images. Various technologies have made the generation of multiparametric imaging files highly feasible although efficient analysis and utilization of this huge amount of data remains a challenge. Multimodality (i.e. transmission, scattering and fluorescence), functional flexibility (i.e. operation as conventional flow cytometry or IFC or 3D-IFC at users' choice), and compatibility with cell sorting are among the three principal areas of development for 3D-IFC to gain wide acceptance as a workhorse for biomedical research and clinical applications.

References

1. Fulwyler MJ (1965) Electronic separation of biological cells by volume. *Science* 150(3698):910–911.

2. Hulett HR, Bonner WA, Barrett J, Herzenberg LA (1969) Cell Sorting: Automated Separation of Mammalian Cells as a Function of Intracellular Fluorescence. *Science* 166:747–749.

3. Cho SH, Godin JM, Chen C-H, Qiao W, Lee H, Lo Y-H (2010) Review Article: Recent advancements in optofluidic flow cytometer. *Biomicrofluidics* 4:043001.

4. Jiang L, Tixeira R, Caruso S, Atkin-Smith GK, Baxter A a, Paone S, Hulett MD, Poon IKH (2016) Monitoring the progression of cell death and the disassembly of dying cells by flow cytometry. *Nat Protoc* 11(4):655–663.

5. Laerum OD, Farsund T (1981) Clinical application of flow cytometry: a review. *Cytometry* 2(1):1–13.

6. Perfetto SP, Chattopadhyay PK, Roederer M (2004) Seventeen-colour flow cytometry: unravelling the immune system. *Nat Rev Immunol* 4(8):648–55.

7. Lugli E, Roederer M, Cossarizza A (2010) Data analysis in flow cytometry: the future just started. *Cytom Part A* 77(7):705–713.

8. Aghaeepour N, Finak G, FlowCAP Consortium, DREAM Consortium, Hoos H, Mosmann TR, Brinkman R, Gottardo R, Scheuermann RH (2013) Critical assessment of automated flow cytometry data analysis techniques. *Nat Methods* 10(3):228–238.

9. Pedreira CE, Costa ES, Lecrevisse Q, van Dongen JJM, Orfao A (2013) Overview of clinical flow cytometry data analysis: Recent advances and future challenges. *Trends Biotechnol* 31(7):415–425.

10. Kay DB, Cambier JL, Wheeless LL (1979) Imaging in flow. *J Histochem Cytochem* 27(1):329–334.

11. Kachel V, Benker G, Lichtnau K, Valet G, Glossner E (1979) Fast imaging in flow: a means of combining flow-cytometry and image analysis. *J Histochem Cytochem* 27(1):335–341.

12. Cambier JL, Kay DB, Wheeless LL (1979) A multidimensional slit-scan flow system. *J Histochem Cytochem* 27:321–324.

13. Kamentsky LA (1979) Future Directions for Flow Cytometry. *J Histochem Cytochem* 27(12):1649–1651.

14. Herzenberg L a., Parks D, Sahaf B, Perez O, Roederer M, Herzenberg L a. (2002) The history and future of the Fluorescence Activated Cell Sorter and flow cytometry: A view from Stanford. *Clin Chem* 48(10):1819–1827.

15. Barteneva NS, Fasler-Kan E, Vorobjev I a. (2012) Imaging Flow Cytometry: Coping with Heterogeneity in Biological Systems. *J Histochem Cytochem* 60(10):723–733.

16. Forment J V, Jackson SP (2015) A flow cytometry-based method to simplify the analysis and quantification of protein association to chromatin in mammalian cells. *Nat Protoc* 10(9):1297–307.

17. Samsel L, Dagur PK, Raghavachari N, Seamon C, Kato GJ, McCoy JP (2013) Imaging flow cytometry for morphologic and phenotypic characterization of rare circulating endothelial cells. *Cytom Part B - Clin Cytom* 84(6):379–389.

18. Headland SE, Jones HR, D'Sa AS V, Perretti M, Norling L V (2014) Cutting-edge analysis of extracellular microparticles using ImageStream(X) imaging flow cytometry. *Sci Rep* 4:5237.

19. Darzynkiewicz Z, Bedner E, Li X, Gorczyca W, Melamed MR (1999) Laser-scanning cytometry: a new instrumentation with many applications. *Exp Cell Res* 249(1):1–12.

20. Pozarowski P, Holden E, Darzynkiewicz Z (2006) Laser Scanning Cytometry: Principles and Applications. *Methods Mol Biol* 319:165–192.

21. Harnett MM (2007) Laser scanning cytometry: understanding the immune system in situ. *Nat Rev Immunol* 7(11):897–904.

22. Henriksen M (2010) Quantitative imaging cytometry : instrumentation of choice for automated cellular and tissue analysis. *Nat Methods* 7(4):i–ii.

23. Pozarowski P, Holden E, Darzynkiewicz Z (2013) Laser Scanning Cytometry: Principles and Applications--An Update. *Methods Mol Biol* 931:187–212.

24. Hutcheson J a., Khan FZ, Powless AJ, Benson D, Hunter C, Fritsch I, Muldoon TJ (2016) A light sheet confocal microscope for image cytometry with a variable linear slit detector. *Proc. of SPIE*, p 97200U.

25. Oheim M (2011) Advances and challenges in high-throughput microscopy for live-cell subcellular imaging. *Expert Opin Drug Discov* 6(12):1299–1315.

26. Zhu H, Mavandadi S, Coskun AF, Yaglidere O, Ozcan A (2011) Optofluidic fluorescent imaging cytometry on a cell phone. *Anal Chem* 83(17):6641–7.

27. Cui X, Lee LM, Heng X, Zhong W, Sternberg PW, Psaltis D, Yang C (2008)

Lensless high-resolution on-chip optofluidic microscopes for Caenorhabditis elegans and cell imaging. *Proc Natl Acad Sci USA* 105(31):10670–5.

28. Wei Q, McLeod E, Qi H, Wan Z, Sun R, Ozcan A (2013) On-chip cytometry using plasmonic nanoparticle enhanced lensfree holography. *Sci Rep* 3:1699.

29. Bishara W, Isikman SO, Ozcan A (2012) Lensfree optofluidic microscopy and tomography. *Ann Biomed Eng* 40(2):251–62.

30. Cheung MC, McKenna B, Wang SS, Wolf D, Ehrlich DJ (2015) Image-based cell-resolved screening assays in flow. *Cytom Part A* 87(6):541–548.

31. McKenna BK, Evans JG, Cheung MC, Ehrlich DJ (2011) A parallel microfluidic flow cytometer for high-content screening. *Nat Methods* 8(5):401–403.

32. Basiji DA, Ortyn WE, Liang L, Venkatachalam V, Morrissey P (2007) Cellular image analysis and imaging by flow cytometry. *Clin Lab Med* 27(3):653–70, viii.

33. Mcgrath KE, Bushnell TP, Palis J (2008) Multispectral Imaging of Hematopoietic Cells: Where Flow Meets Morphology. *J Immunol Methods* 336(2):91–97.

34. Vorobjev IA, Barteneva NS (2016) *Imaging Flow Cytometry Methods and protocols* eds Barteneva NS, Vorobjev IA (Springer Science+Business Media).

35. Cho SH, Chen CH, Tsai FS, Godin JM, Lo Y-H (2010) Human mammalian cell sorting using a highly integrated micro-fabricated fluorescence-activated cell sorter (microFACS). *Lab Chip* 10(12):1567–1573.

36. Schmid L, Weitz D a., Franke T (2014) Sorting drops and cells with acoustics: acoustic microfluidic fluorescence-activated cell sorter. *Lab Chip* 14(19):3710–3718.

37. Ren L, Chen Y, Li P, Mao Z, Huang P-H, Rufo J, Guo F, Wang L, McCoy JP, Levine SJ, Huang TJ (2015) A high-throughput acoustic cell sorter. *Lab Chip* 15(19):3870–3879.

38. Shields CW, Reyes CD, López GP (2015) Microfluidic cell sorting: a review of the advances in the separation of cells from debulking to rare cell isolation. *Lab Chip* 15(5):1230–49.

39. Elliott GS (2009) Moving pictures: imaging flow cytometry for drug development. *Comb Chem High Throughput Screen* 12(9):849–59.

40. EMD Millipore (2012) INSPIRE ®. (August):18.

41. Schonbrun E, Gorthi SS, Schaak D (2012) Microfabricated multiple field of view imaging flow cytometry. *Lab Chip* 12(2):268–73.

42. Gorthi SS, Schaak D, Schonbrun E (2013) Fluorescence imaging of flowing cells using a temporally coded excitation. *Opt Express* 21(4):5164–70.

43. Goda K, Tsia KK, Jalali B (2009) Serial time-encoded amplified imaging for real-time observation of fast dynamic phenomena. *Nature* 458(7242):1145–1149.

44. Goda K, Motafakker-Fard A, Tsia KK, Jalali B (2010) Serial Time Encoded Amplified Microscopy (STEAM) for high-throughput detection of rare cells. *IEEE Photonics Society Winter Topicals Meeting Series*, p TuB2.2.

45. Goda K, Ayazi A, Gossett DR, Sadasivam J, Lonappan CK, Sollier E, Fard AM, Hur SC, Adam J, Murray C, Wang C, Brackbill N, Di Carlo D, Jalali B (2012) High-throughput single-microparticle imaging flow analyzer. *Proc Natl Acad Sci USA* 109(29):11630–5.

46. Huang E, Ma Q, Liu Z (2016) Ultrafast Imaging using Spectral Resonance Modulation. *Sci Rep* 6:25240.

47. Mahjoubfar A, Chen C, Niazi KR, Rabizadeh S, Jalali B (2013) Label-free high-throughput cell screening in flow. *Biomed Opt Express* 4(9):1618–25.

48. Lau AKS, Shum HC, Wong KKY, Tsia KK (2016) Optofluidic time-stretch imaging – an emerging tool for high-throughput imaging flow cytometry. *Lab Chip* 16:1743–1756.

49. Ugawa M, Lei C, Nozawa T, Ideguchi T, Carlo D Di, Ota S, Ozeki Y, Goda K (2015) High-throughput optofluidic particle profiling with morphological and chemical specificity. *Opt Lett* 40(20):4803–6.

50. Lei C, Ugawa M, Nozawa T, Ideguchi T, Di Carlo D, Ota S, Ozeki Y, Goda K (2016) High-throughput time-stretch microscopy with morphological and chemical specificity. *Proc. of SPIE*, p 97200X.

51. Diebold ED, Buckley BW, Gossett DR, Jalali B (2013) Digitally synthesized beat frequency multiplexing for sub-millisecond fluorescence microscopy. *Nat Photonics* 7(10):806–810.

52. Mikami H, Kobayashi H, Hamad S, Ozeki Y, Goda K (2016) Ultrafast Confocal Fluorescence Microscopy by Frequency-Division-Multiplexed Multi-Line Focusing. *CLEO*, p AM4O.5.

53. Mikami H, Kobayashi H, Wang Y, Hamad S, Ozeki Y, Goda K (2016) Enhanced speed in fluorescence imaging using beat frequency multiplexing. *Proc. of SPIE*, p 97200T.

54. Lang P, Yeow K, Nichols A, Scheer A (2006) Cellular imaging in drug discovery. *Nat Rev Drug Discov* 5(4):343–356.

55. Wollman R, Stuurman N (2007) High throughput microscopy: from raw images to discoveries. *J Cell Sci* 120:3715–3722.

56. Tse HTK, Meng P, Gossett DR, Irturk A, Kastner R, Di Carlo D (2011) Strategies for Implementing Hardware-Assisted High-Throughput Cellular Image Analysis. *J Lab Autom* 16(6):422–430.

57. Henery S, George T, Hall B, Basiji D, Ortyn W, Morrissey P (2008) Quantitative image based apoptotic index measurement using multispectral imaging flow cytometry: A comparison with standard photometric methods. *Apoptosis* 13(8):1054–1063.

58. George TC, Fanning SL, Fitzgeral-Bocarsly P, Medeiros RB, Highfill S, Shimizu Y, Hall BE, Frost K, Basiji D, Ortyn WE, Morrissey PJ, Lynch DH (2006) Quantitative measurement of nuclear translocation events using similarity analysis of multispectral cellular images obtained in flow. *J Immunol Methods* 311(1–2):117–129.

59. Hayashi M, Hattori A, Kim H, Terazono H, Kaneko T, Yasuda K (2011) Fully automated on-chip imaging flow cytometry system with disposable contamination-free plastic re-cultivation chip. *Int J Mol Sci* 12(6):3618–3634.

60. Han Y, Lo Y-H (2015) Imaging Cells in Flow Cytometer Using Spatial-Temporal Transformation. *Sci Rep* 5(1):13267.

61. Frankowski M, Theisen J, Kummrow A, Simon P, Ragusch H, Bock N, Schmidt M, Neukammer J (2013) Microflow cytometers with integrated hydrodynamic focusing. *Sensors (Basel)* 13(4):4674–4693.

62. Darzynkiewicz Z, Juan G, Li X, Gorczyca W, Murakami T, Traganos F (1997) Cytometry in cell necrobiology: Analysis of apoptosis and accidental cell death (necrosis). *Cytometry* 27(1):1–20.

63. Schmitt JM, Kumar G (1998) Optical scattering properties of soft tissue: a discrete particle model. *Appl Opt* 37(13):2788–2797.

64. Hielscher a H, Mourant JR, Bigio IJ (1997) Influence of particle size and concentration on the diffuse backscattering of polarized light from tissue phantoms and biological cell suspensions. *Appl Opt* 36(1):125–135.

65. Perelman L, Backman V, Wallace M, Zonios G, Manoharan R, Nusrat a., Shields S, Seiler M, Lima C, Hamano T, Itzkan I, Van Dam J, Crawford J, Feld M (1998) Observation of Periodic Fine Structure in Reflectance from Biological Tissue: A New Technique for Measuring Nuclear Size Distribution. *Phys Rev Lett* 80(3):627–630.

66. Schmitt JM, Kumar G (1996) Turbulent nature of refractive-index variations in

biological tissue. *Opt Lett* 21(16):1310–1312.

67. Wu T-F, Yen TM, Han Y, Chiu Y-J, Lin EY-S, Lo Y-H (2014) A light-sheet microscope compatible with mobile devices for label-free intracellular imaging and biosensing. *Lab Chip* 14(17):3341–3348.

68. Altschuler SJ, Wu LF (2010) Cellular heterogeneity: do differences make a difference? *Cell* 141(4):559–63.

69. Snijder B, Pelkmans L (2011) Origins of regulated cell-to-cell variability. *Nat Rev Mol Cell Biol* 12(2):119–125.

70. Almendro V, Marusyk A, Polyak K (2013) Cellular Heterogeneity and Molecular Evolution in Cancer. *Annu Rev Pathol Mech Dis* 8(1):277–302.

71. Pelkmans L (2012) Using Cell-to-Cell Variability--A New Era in Molecular Biology. *Science* 336(6080):425–426.

72. Laerum OD, Farsund T (1981) Clinical application of flow cytometry: A review. *Cytometry* 2(1):1–13.

73. Telford WG, Hawley T, Subach F, Verkhusha V, Hawley RG (2012) Flow cytometry of fluorescent proteins. *Methods* 57(3):318–330.

74. Barteneva NS, Fasler-Kan E, Vorobjev IA (2012) Imaging flow cytometry: coping with heterogeneity in biological systems. *J Histochem Cytochem* 60(10):723–33.

75. Basiji DA, Ortyn WE, Liang L, Venkatachalam V, Morrissey P (2007) Cellular Image Analysis and Imaging by Flow Cytometry. *Clin Lab Med* 27(3):653–viii.

76. Han Y, Gu Y, Zhang AC, Lo Y-H (2016) Review: imaging technologies for flow cytometry. *Lab Chip* 16(24):4639–4647.

77. Huang F, Sirinakis G, Allgeyer ES, Schroeder LK, Duim WC, Kromann EB, Phan T, Rivera-Molina FE, Myers JR, Irnov I, Lessard M, Zhang Y, Handel MA, Jacobs-Wagner C, Lusk CP, Rothman JE, Toomre D, Booth MJ, Bewersdorf J (2016) Ultra-High Resolution 3D Imaging of Whole Cells. *Cell* 166(4):1028–1040.

78. Conchello J-A, Lichtman JW (2005) Optical sectioning microscopy. *Nat Methods* 2(12):920–931.

79. Pitrone PG, Schindelin J, Stuyvenberg L, Preibisch S, Weber M, Eliceiri KW, Huisken J, Tomancak P (2013) OpenSPIM: an open-access light-sheet microscopy platform. *Nat Methods* 10(7):598–599.

80. Dada OO, Huge BJ, Dovichi NJ (2012) Simplified sheath flow cuvette design for

ultrasensitive laser induced fluorescence detection in capillary electrophoresis. *Analyst* 137(13):3099–101.

81. Ling JQ, Li T, Hu JF, Vu TH, Chen HL, Qiu XW, Cherry AM, Hoffman AR (2006) CTCF mediates interchromosomal colocalization between Igf2/H19 and Wsb1/Nf1. *Science* 312(5771):269–72.

82. Mueller F, Senecal A, Tantale K, Marie-Nelly H, Ly N, Collin O, Basyuk E, Bertrand E, Darzacq X, Zimmer C (2013) FISH-quant: automatic counting of transcripts in 3D FISH images. *Nat Methods* 10(4):277–278.

83. Dickey JS, Redon CE, Nakamura AJ, Baird BJ, Sedelnikova OA, Bonner WM (2009) H2AX: functional roles and potential applications. *Chromosoma* 118(6):683–692.

84. Ivashkevich A, Redon CE, Nakamura AJ, Martin RF, Martin OA (2012) Use of the γ-H2AX assay to monitor DNA damage and repair in translational cancer research. *Cancer Lett* 327(1–2):123–133.

85. Hagiwara Y, Niimi A, Isono M, Yamauchi M, Yasuhara T, Limsirichaikul S, Oike T, Sato H, Held KD, Nakano T, Shibata A, Hagiwara Y, Niimi A, Isono M, Yamauchi M, Yasuhara T, Limsirichaikul S, Oike T, Sato H, et al. (2017) 3D-structured illumination microscopy reveals clustered DNA double-strand break formation in widespread γH2AX foci after high LET heavy-ion particle radiation. *Oncotarget* 8(65):109370–109381.

86. Zhang Q, Zhong L, Tang P, Yuan Y, Liu S, Tian J, Lu X (2017) Quantitative refractive index distribution of single cell by combining phase-shifting interferometry and AFM imaging. *Sci Rep* 7(1):2532.

87. Liu PY, Chin LK, Ser W, Chen HF, Hsieh C-M, Lee C-H, Sung K-B, Ayi TC, Yap PH, Liedberg B, Wang K, Bourouina T, Leprince-Wang Y (2016) Cell refractive index for cell biology and disease diagnosis: past, present and future. *Lab Chip* 16(4):634–644.

88. Chang JT, Palanivel1 VR, Kinjyo I, Schambach F, Intlekofer AM, Banerjee A, Longworth1 SA, Vinup KE, Mrass P, Oliaro J, Killeen N, Orange JS, Russell SM, Weninger W, Reiner SL (2007) Asymmetric T Lymphocyte Division in the Initiation of Adaptive Immune Responses. *Science* 315(5819):1187–1191.

89. Roberts JP, Tesdorpf J (2015) *Phenotypic Drug Discovery with High Content Screening* Available at: www.perkinelmer.com [Accessed January 6, 2019].

90. Heath JR, Ribas A, Mischel PS (2016) Single-cell analysis tools for drug discovery and development. *Nat Rev Drug Discov* 15(3):204–16.

91. Amara JF, Cheng SH, Smith AE (1992) Intracellular protein trafficking defects in

human disease. *Trends Cell Biol* 2(5):145–149.

92. Gomez-Navarro N, Miller E (2016) Protein sorting at the ER-Golgi interface. *J Cell Biol* 215(6):769–778.

93. Olkkonen VM, Ikonen E (2006) When intracellular logistics fails--genetic defects in membrane trafficking. *J Cell Sci* 119(Pt 24):5031–45.

94. Janssen A, Burg M van der, Szuhai K, Kops GJPL, Medema RH (2011) Chromosome Segregation Errors as a Cause of DNA Damage and Structural Chromosome Aberrations. *Science* 333(6051):1895–8.

95. Ota S, Horisaki R, Kawamura Y, Ugawa M, Sato I, Hashimoto K, Kamesawa R, Setoyama K, Yamaguchi S, Fujiu K, Waki K, Noji H (2018) Ghost cytometry. *Science* 360(6394):1246–1251.

96. Nitta N, Sugimura T, Isozaki A, Mikami H, Hiraki K, Sakuma S, Iino T, Arai F, Endo T, Fujiwaki Y, Fukuzawa H, Hase M, Hayakawa T, Hiramatsu K, Hoshino Y, Inaba M, Ito T, Karakawa H, Kasai Y, et al. (2018) Intelligent Image-Activated Cell Sorting. *Cell* 175(1):266–276.e13.

97. Marx V (2013) Biology: The big challenges of big data. *Nature* 498(7453):255–260.

98. May M (2014) LIFE SCIENCE TECHNOLOGIES: Big biological impacts from big data. *Science* 344(6189):1298–1300.

99. Gossett DR, Tse HTK, Lee S a., Ying Y, Lindgren a. G, Yang OO, Rao J, Clark a. T, Di Carlo D (2012) Hydrodynamic stretching of single cells for large population mechanical phenotyping. *Proc Natl Acad Sci* 109(20):7630–7635.

100. Zheng Y, Nguyen J, Wei Y, Sun Y (2013) Recent advances in microfluidic techniques for single-cell biophysical characterization. *Lab Chip* 13(13):2464–83.

101. Galler K, Bräutigam K, Grosse C, Popp J, Neugebauer U (2014) Making a big thing of a small cell--recent advances in single cell analysis. *Analyst* 139(6):1237–1273.

102. Blasi T, Hennig H, Summers HD, Theis FJ, Cerveira J, Patterson JO, Davies D, Filby A, Carpenter AE, Rees P (2016) Label-free cell cycle analysis for high-throughput imaging flow cytometry. *Nat Commun* 7:10256.

103. Chen CL, Mahjoubfar A, Tai L-C, Blaby IK, Huang A, Niazi KR, Jalali B (2016) Deep Learning in Label-free Cell Classification. *Sci Rep* 6(August 2015):21471.

104. Bosworth BT, Foster MA (2013) High-speed ultrawideband photonically enabled compressed sensing of sparse radio frequency signals. *Opt Lett* 38(22):4892–4895.

105. Bosworth BT, Stroud JR, Tran DN, Tran TD, Chin S, Foster MA (2015) Continuous high-rate photonically-enabled compressed sensing (CHiRP-CS) for high speed flow microscopy. *Imaging Appl Opt*:OSA Technical Digest (online)

106. Zhang AC, Gu Y, Han Y, Mei Z, Chiu Y-J, Geng L, Cho SH, Lo Y-H (2016) Computational cell analysis for label-free detection of cell properties in a microfluidic laminar flow. *Analyst* 141:4142–4150.